Check for updates

Synergistically enhanced single-atomic site catalysts for clean energy conversion

Fa Yang [abc] and Weilin Xu [*ac]

The development of cost-effective, high-performance catalysts at the atomic level has become a challenging issue for large-scale applications of renewable clean energy conversion. With adjustable structural characteristics and maximum atomic utilization efficiency, single-atomic site catalysts (SACs) are considered to be the most potential next-generation materials. Moreover, the introduction and coupling of some synergistic components is desirable to accurately regulate the structural interactions and lead to improved activity. In addition to the strong metal–support interaction (SMSI) in SACs, there is tremendous opportunity to explore and develop the synergistic effect of SAC-nanoparticles (SAC-NPs), SAC-clusters (SACCs), dual-atom site catalysts (DACs), and single-atomic alloys (SAAs). Moreover, these unique synergistic structures between adjacent atomic sites could still maintain their high atomically dispersed nature and stability. In this review, we begin by introducing the types, synthetic strategies and characterization methods of SAC-NPs, SACCs, DACs and SAAs, discussing the key factors controlling their structures. We then review several important clean energy catalytic reactions performed over these atomic-coupling structures, and compare the respective advantages and disadvantages of SACs, SAC-NPs, SACCs, DACs and SAAs. Finally, the challenges and perspectives of this unique single-atomic site synergistic effect are suggested. We believe that this critical review provides guidance for the rational design of new single-atomic site catalysts for clean energy conversion.

[a]State Key Laboratory of Electroanalytical Chemistry, Jilin Province Key Laboratory of Low Carbon Chemical Power, Changchun Institute of Applied Chemistry, Chinese Academy of Sciences, Changchun 130022, China. E-mail: weilinxu@ciac.ac.cn

[b]Key Laboratory of the Ministry of Education for Advanced Catalysis Materials, College of Chemistry and Life Sciences, Zhejiang Normal University, Jinhua 321004, China. E-mail: yangfa@zjnu.edu.cn

[c]University of Science and Technology of China, Hefei, Anhui 230026, China

1. Introduction

The increasing concerns of climate pollution and energy crisis make it imperative to accelerate the development of sustainable energy storage and clean conversion, such as fuel cells, electrocatalysis, supercapacitors and various batteries.[1–3] Generally, electrochemical reactions are at the core of these energy

Fa Yang received his PhD degree from the University of Science and Technology of China and Changchun Institute of Applied Chemistry (CIAC), Chinese Academy of Sciences in 2020, and then he worked at Zhejiang Normal University as a Distinguished Professor. His research studies focus on CO₂ electro-reduction and in situ spectro-electrochemistry (ATR-IR and SERS).
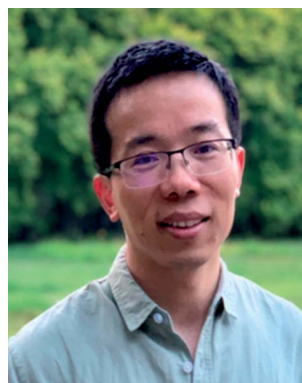
Prof. Weilin Xu received his PhD degree from Changchun Institute of Applied Chemistry (CIAC), Chinese Academy of Sciences in 2006. He did postdoc research at Cornell University, UC Berkeley and the Lawrence Berkeley National Lab from 2007 to 2011. After that, he built his own research group in CIAC by focusing on energy-process related basic and practical research, including single-molecule nanocatalysis, development of functional materials for the oxygen reduction reaction (ORR), oxygen-evolution reaction (OER), hydrogen-evolution reaction (HER), CO₂ reduction reaction (CO₂RR) and nitrogen reduction reaction (NRR).

This journal is © The Royal Society of Chemistry 2022

J. Mater. Chem. A, 2022, **10**, 5673–5698 | **5673**

conversion and storage systems, involving the hydrogen evolution reaction (HER), oxygen reduction reaction (ORR), oxygen evolution reaction (OER), carbon dioxide reduction reaction (CO_2RR), nitrogen reduction reaction (N_2RR), and so on.[4–6] However, most of these chemical transformation processes demand highly efficient catalysts to lower the energy barrier and facilitate the kinetics of the reactions. Single-atomic site catalysts (SACs) have been attracting wide attention due to their maximal atom utilization, well-defined active centers, uniform activity for each active site, conformational flexibility, unique electronic structure and tunable intrinsic selectivity toward various reactions compared with their counterpart clusters and nanoparticles.[7,8] In addition, SACs can be used to establish the relationship between catalytic activity with atomic coordination environment, and their quantum size effects create discrete energy-level distribution and distinctive HOMO–LUMO gaps, and bring new opportunities to the study of molecular and atomic catalytic mechanisms by tailoring the coordination state.[9,10]

Despite the broad application prospect of single-atomic catalysis, SACs suffer from structural simplicity and lack of synergistic active sites for surpassing the intrinsic performance limit of more complicated electrocatalytic reactions. On one hand, owing to the presence of only one kind of specific active site in most of the SACs, it is difficult to break the linear scaling relationships between the adsorption energies of overall complicated reactions involving multiple intermediates, and not effective towards some reactions.[11] This is mainly because SACs could only activate one of the elementary reaction steps. For instance, the structural simplicity of single atomic centers limits the reactivity of the multistep coupled proton–electron transfer CO_2RR process.[12–14] Iron (Fe) and cobalt (Co) based SACs generally show a lower CO_2RR onset potential, but *CO is difficult to desorb owing to the strong binding of the Fe or Co site with reaction intermediates.[15] Nickel (Ni) and copper (Cu) based SACs facilitate CO desorption, but they are often limited by a larger initial potential due to the high energy barrier required to form the *COOH intermediate.[16,17] In addition, the too strong binding strength of transition metal (TM) sites with electron-donating intermediates also lowers the catalytic activity of OER and HER processes.[18] On the other hand, to maintain the single-atom configuration, the loading amount of metals is often limited to avoid aggregation (usually ~1 wt%). Hence, the overall activity of SACs is not very remarkable in spite of high activity per atom. Moreover, increasing the surface free energy of only one kind of single metal site tends to cause agglomeration of SACs, resulting in a significant decline in performance.[19,20]

Coupling multi-active sites into one catalyst for multi-step reactions is a direct strategy to compensate these drawbacks of SACs by synergic catalysis. However, it is still rather tough to design multi-active site catalysts. Generally, the activity of SACs can be effectively tuned by the rational design of coordination configurations, including the type/state of metal-atomic centers and surrounding coordination environment.[21,22] It is worth noting that the strong metal–support interaction (SMSI) is relatively common in SAC catalysis, and the modulation of SMSI

Fig. 1 Schematic illustration of synergistically enhanced single-atomic sites for electrocatalysis.

will affect their geometric and electronic properties to improve reaction path appropriately. Inspired by this, some synergistic components, such as local coordination atoms, heteroatoms and other metal atoms, have been developed to modulate the local environment of SACs.[23–25] What's more noteworthy is that the introduction of some metal-based nanoparticles, nanoclusters, and/or diatomic sites makes it effective to improve the reactivity of SACs. Besides, the strong interactions between active metal centers and adjacent atoms could enhance the catalytic activity, selectivity and durability of metal centers while still maintaining the high atomic dispersion property and stability.[26–28] Therefore, it is urgent and promising to establish and explore the synergistic effect of SAC-nanoparticles (SAC-NPs), SAC-clusters (SACCs), dual-atomic site catalysts (DACs), and single-atomic alloys (SAAs). However, there's still a lot of controversy about the synergistic mechanism and the nature of catalytic processes (Fig. 1).

Since the concept of SACs was put forth in 2011, this field has progressed rapidly in the construction of SACs and energy-related applications.[29] To date, most review articles focus on the design strategies of SACs and the impact of atomic engineering methods on their intrinsic activities and stabilities. In fact, the introduction and coupling of some synergistic components, including SAC-NPs, SACCs, DACs and SAAs, are more desirable to accurately tune the relationships of the atomic structure and coordination environment with reactivity, but a comprehensive and timely review of synergistically enhanced single-atomic catalysis for clean energy conversion is still lacking.[30,31] In this review, we will thus first describe the classifications and synthesis methods of SAC-NPs, SACCs, DACs and SAAs, discussing the key factors controlling their synergistic structure, and identifying the main challenges for catalyst design. Then, we briefly summarize and comment on the advantages and limitations of some important and recently developed characterization techniques in determining the unique coordination structure, including the high-angle annular dark-field scanning transmission electron microscopy (HAADF-STEM) equipped with energy dispersive X-ray spectroscopy (EDS) and electron energy loss spectroscopy (EELS), X-ray absorption near edge

5674 | *J. Mater. Chem. A*, 2022, **10**, 5673–5698

This journal is © The Royal Society of Chemistry 2022

spectroscopy (XANES), extended X-ray absorption fine structure (EXAFS) analysis, *in situ* ambient-pressure XPS (AP-XPS), IR and Raman spectroscopies, and Mössbauer spectroscopy. It is thus vital to apply more than one technique to fully characterize their coordination structures before establishing conclusive mechanisms. After that, a detailed comparison, analysis and evaluation of these atomic-coupling structures (SAC-NPs, SACCs, DACs and SAAs) in energy storage and conversion applications will be made, including the ORR, HER, OER, CO_2RR, and N_2RR. Finally, the promising prospects and tough challenges of this unique single-atomic site synergistic effect will be proposed. We believe that this review could provide new insights for readers and inspire more efforts on the rational design and comprehension of the newly developed single-atomic site catalysts, facilitating the rapid development in this synergistic catalysis frontier.

2. Categories and synthesis of atomic-coupling structures

Based on the difference in the synergistic effect, adjacent metal species, coordination environments, and electronic structures, single atomic-coupling structures are generally categorized into four types: SAC-NPs, SACCs, DACs and SAAs. Notably, the distance range between different adjacent objects also plays an important role in defining these atomic-coupling structures. For example, Lu *et al.* showed that a Pt_2 DAC could be fabricated based on Pt_1 single-atom deposition. According to their observation, Pt_1 single atoms were isolated from each other by a distance >2 nm in average, which is significantly larger than the diameter of the precursor molecule ($MeCpPtMe_3$), ∼0.96 nm, confirming the steric effect during the synthesis.[32] Li *et al.* synthesized highly dispersed Fe_2 clusters supported on mesoporous carbon nitride (Fe_2/mpg-C_3N_4). The statistical analysis of 100 pairs of Fe_2 dimers shows that the projected Fe–Fe distance between adjacent atoms varies from 0.12 to 0.25 nm, while the largest distance is consistent with the bond length of an Fe_2 DAC.[33] Besides, Cheng *et al.* constructed a Ru atomically dispersed catalyst with Ru–C_5 single atoms and Ru oxide nanoclusters (∼1.5 nm), the distance between Ru nanoclusters and Ru single atoms being ∼0.3 nm. Such a short distance may lead to the nanocluster being in close cooperation with the single atoms, further enhancing the catalytic performance.[34] In addition, diverse coupling/coordination structures and bonding nature of single-atomic sites may bring new opportunities to establish atomic multisite catalysts, lead to highly efficient charge and mass transfers for multistep electrocatalytic reactions. This is a truly distinctive feature of SACs that distinguishes it from other conventional electrocatalysts. However, these multisite catalysts involving atomically dispersed active sites are hard to construct due to the close-packed structure of metals and strong interaction between different atoms. In this section, various types of SACs and their synthesis methods, including multi-step pyrolysis, wet-chemical, impregnation/immersion method, chemical vapor deposition (CVD), atomic layer deposition (ALD), electrodeposition, sequential reduction, dealloying, galvanic replacement, and proton-capture strategy, are summarized in detail.

2.1 Single atomic site-nanoparticles (SAC-NPs)

It is well known that the size effect of metals remains complicated, and smaller metal species (atomically dispersed sites) do not necessarily improve the reactivity significantly.[35] In this context, metallic nanoparticles could act as synergistic active sites in conjunction with SAC configurations to accelerate the reaction process. However, it is a great challenge to simultaneously acquire high-concentration single-atomic and metal nanosized species in the same catalyst due to the high competition that exists during preparation. To the best of our knowledge, currently, most of the reported SAC-NPs could be roughly divided into two categories: M_{NPs}/M_{SAC}–N–C and M@C–M_{SAC}.[36] For example, Wu *et al.* reported an effective approach to design a kind of uniform and fine Pt nanoparticle (∼2 nm) dispersion on FeN_4 site-rich carbon (Pt/FeN_4–C),[37] the specific synthesis process is shown in Fig. 2a. In short, they firstly attempted chemical doping of Fe^{3+} ions into ZIF-8 nanocrystal precursors to form FeN_4–C, and to load Pt or PtCo nanoparticles by high temperature graphitization. Ye *et al.* developed a low-temperature chemical vapor deposition strategy to prepare a sheet-like open nanostructure with Ni nanoparticles wrapped by Ni-NC species (Ni-NC/Ni).[38] In addition, Hou *et al.* proposed a proton capture strategy to prepare a hybrid catalyst containing Ni NPs supported by a carbon matrix with atomically dispersed Ni–N_x sites (denoted as Ni-NiNCM).[39] As for the type of M@C_{NPs}–M_{SAC}, for instance, Mai *et al.* reported bimetallic zeolitic imidazole framework (BMZIF)-derived carbon spheres with graphene-encapsulated Co nanoparticles (Co@C) and isolated single Co atoms (CoSAs), denoted as Co-NCS.[40] As shown in Fig. 2b, the resin microspheres with abundant functional groups could absorb Zn/Co ions and provide adequate structural support after carbonization, which prevents the aggregation of nanocrystal precursors. Moreover, the introduction of Zn^{2+} could disperse Co species due to the evaporation of Zn at high temperatures. John *et al.* also combined isolated Mo single atoms with Mo carbide particles (Mo_2C–MoSAs) by two-stage heat treatment.[41] Recently, Christopher and Yang *et al.* adopted a new strategy to simultaneously craft single-atomic Fe sites and graphitic layer-wrapped Fe_3C nanoparticles (Fe_3C@GLNPs) encapsulated within hollow mesoporous carbon tubes through hydrothermally self-templated polyimide tubes (PITs),[42] as illustrated in Fig. 2c. Therefore, the integration of independent single-atom and nanosized metal species in the same material represents a promising route to improve the reactivity.

2.2 Single atomic site-clusters (SACCs)

Atomically dispersed catalysts (ADCs), such as clusters and single atomic sites, received great attention due to their individual coordination environments and ultra-high atomic utilization. Notably, diverse coordination structures of ADCs may provide opportunity for the construction of atomic multisite catalysts. Moreover, the catalytic pathway and reactivity may differ considerably depending on the form of active site. Coupling multi-active sites into one material for a multi-step reaction process is a direct way to compensate the drawback of single-site catalysts. However, it is rather difficult to assemble multiple
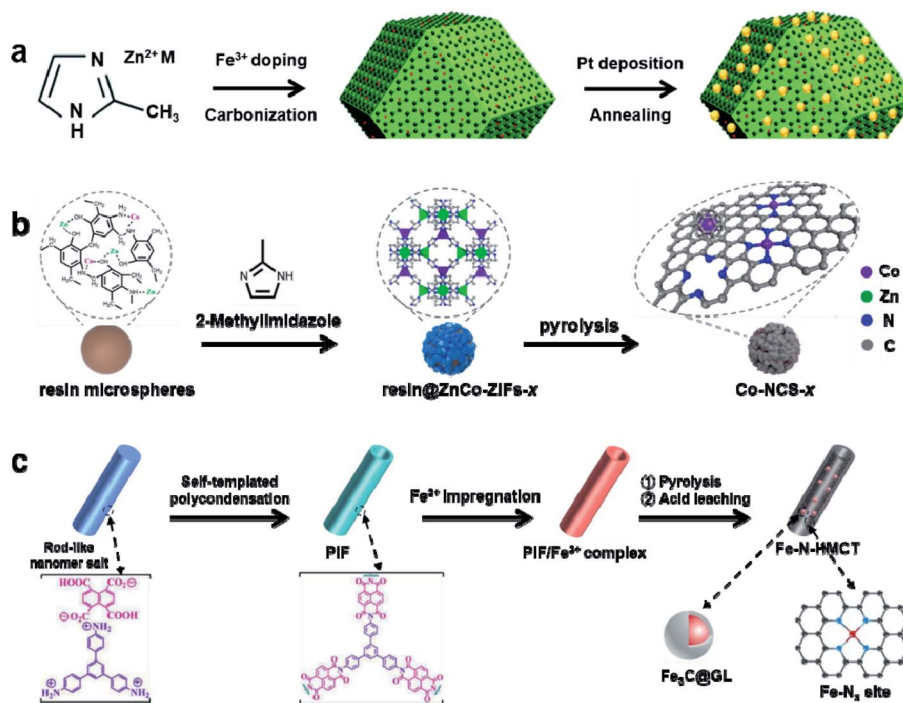
This journal is © The Royal Society of Chemistry 2022

J. Mater. Chem. A, 2022, **10**, 5673–5698 | **5675**

Fig. 2 (a) Synthesis scheme of the FeN_4–C derived carbon-supported Pt or PtCo catalysts. Reproduced from ref. 37 with permission from the Royal Society of Chemistry, copyright 2021. (b) Schematic illustration of the synthesis process of Co-NCS-*x*. Reproduced from ref. 40 with permission from Elsevier Ltd, Copyright 2021. (c) Schematic illustration for the synthesis of Fe–N-HMCT catalysts. Reproduced from ref. 42 with permission from Wiley-VCH GmbH, copyright 2020.

active sites into one catalyst. Although various synthetic strategies have been applied to fabricate highly active ADCs, controlled and large-scale synthesis of stable single atoms and clusters remains a considerable challenge due to the natural tendency of metal atoms to diffuse and agglomerate, resulting in the formation of larger particles. For example, high temperature calcination will inevitably cause particle agglomeration in the traditional impregnation–pyrolysis process. Thus, it is urgent to develop a milder and more effective method to synthesize multi-site atomically dispersed catalysts and further understand their corresponding intrinsic synergistic effect. For example, Jiang *et al.* reported a new strategy by integrating vacuum-freeze-drying and high-temperature pyrolysis technologies to design atomically dispersed Co deposits onto the surface of Ru clusters.[43] Cheng *et al.* developed a universal and facile room temperature impregnation strategy to construct a Ru atomically dispersed catalyst with Ru–C_5 single atoms and Ru oxide nanoclusters (~1.5 nm), which could also be extended to prepare Ir, Rh, Pt, Au, and Mo atomically dispersed catalysts.[34]

In addition, atomically dispersed metal sites on carbon, especially those with M–N–C coordination, have demonstrated excellent catalytic activities both experimentally and theoretically.[44,45] Catalysts with combined atomic sites, nanoclusters or even metallic particles have also been regarded as M–N–C catalysts, indicating the feasibility of multiple sites or clusters acting as a secondary active center. However, these synergistic or cooperative active sites consisting of multiple metal sites are not fully understood. Based on this, Nayantara *et al.* fabricated a heterostructured catalyst with the integration of Fe single

atom and Co cluster sites in N-doped graphitic carbon (Fe SAs@Co/N-GC) by using a three-step wet-chemical and thermostatic carbonization process,[46] as shown in Fig. 3a. At present, covalent–organic frameworks (COFs) can also be used as an ideal porous carbon precursor to produce Fe–N–C catalysts. Fe ions can easily diffuse into the cavities of COFs, while the N sites on COFs may act as a ligand to anchor Fe cations. Ao *et al.* employed a size controlled strategy to synthesize an Fe_{AC}@Fe_{SA}–N–C catalyst, in which Fe atomic clusters are embedded in an atomically dispersed Fe–N–C matrix, based on periodic skeletons and separated building blocks of COFs,[47] as illustrated in Fig. 3b. Furthermore, Lawrence *et al.* prepared an Fe single atom/cluster embedded on N-doped carbon (Fe/NC) by the pyrolytic treatment of Fe salts and glucosamine in the presence of porosity-inducing templates (Fig. 3c).[48] Sun *et al.* developed a practical synthesis method to produce isolated single platinum atoms and clusters (ALDPt/NGNs) using the atomic layer deposition technique.[49] We believe that more and more effective SACCs will be designed with the continuous development and improvement of various synthetic strategies.

2.3 Dual-atom site catalysts (DACs)

In contrast to SACs, dual-atomic catalysts (DACs) utilize two adjacent metal atomic species to achieve complementary functionalities and synergy, and the strong chemical interactions between neighboring metal atoms could create highly stable active centers by efficiently stabilizing the individual species. Generally, DACs could be divided into three categories
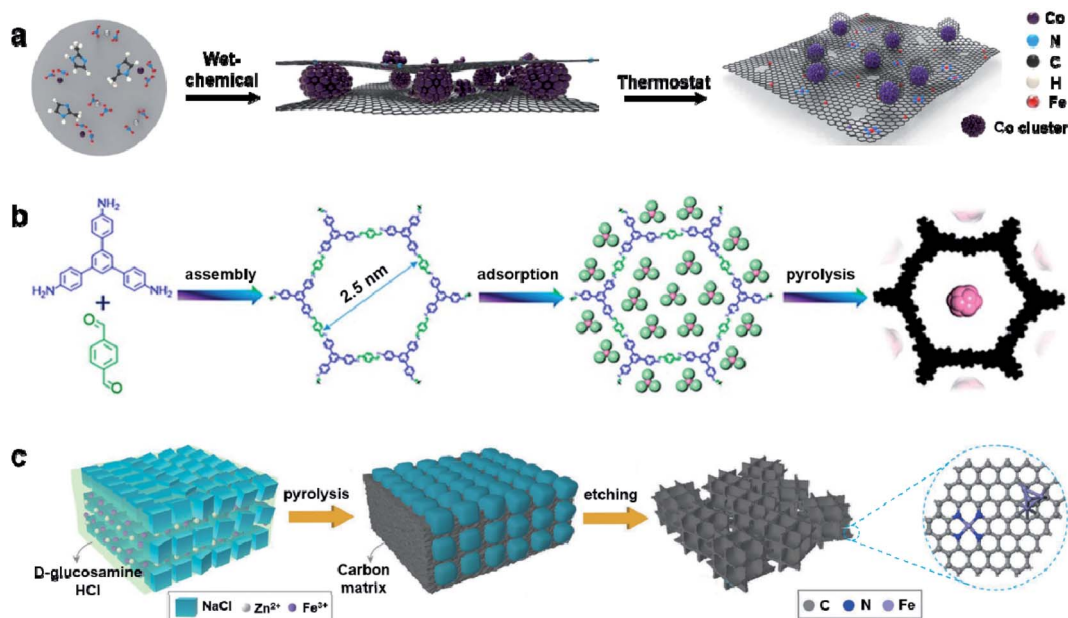
Fig. 3 (a) Fabrication scheme of Fe SAs@Co/N-GC catalysts. Reproduced from ref. 46 with permission from the American Chemical Society, copyright 2021. (b) Illustration of the synthesis process of Fe$_{AC}$@Fe$_{SA}$−N−C. Reproduced from ref. 47 with permission from the American Chemical Society, copyright 2019. (c) Schematic illustration of the synthetic procedures for Fe single atom/nanocluster embedded in N-doped carbon (Fe/NC). The model structure of Fe/NC is shown in the dotted circle. Reproduced from ref. 48 with permission from Wiley-VCH GmbH, copyright 2021.

according to the configuration of active sites: combination of two single-atomic active sites, homonuclear DACs, and heteronuclear DACs.[30,31,50] The first type is composed of two kinds of single-atomic sites randomly dispersed, and few of the two metal atoms (M and M′) are adjacent to each other. In the other two kinds of DACs, most of the two metal atoms are adjacent, even bonded to each other, and the difference is whether the two adjacent metal atoms are the same. Hence, it is more difficult to synthesize homonuclear or heteronuclear DACs due to the difficulty in controlling exact coordination configurations and preventing the aggregation of isolated metal atoms during the synthesis. To achieve this, strong covalent bonds between coordinated atoms are need to lower the free energy of metal dimers. Just like the approaches for the preparation of single-atomic catalysts, bottom-up and top-down strategies are desirable for the synthesis of DACs.

In bottom-up strategies, mono- or multinucleus metal complex precursors are first physically adsorbed and finally chemically reduced and confined in vacancies to form DACs. To date, various bottom-up approaches for DAC preparation have been successfully established, such as atomic layer deposition (ALD), chemical vapor deposition (CVD), impregnation, and electrochemical methods. The ALD and CVD methods are widely used techniques, which deposit metal atoms uniformly on the surface of the support with good repeatability, resulting in precise control of the structure, particle size, and composition. The uniform deposition character of ALD makes it a powerful approach to construct exact bimetallic sites and explore the structure–performance relationship. For example, Yang *et al.* developed a DAC consisting of an O-coordinated W–

Mo heterodimer embedded in N-doped graphene (W$_1$Mo$_1$–NG),[51] which is synthesized by a controllable three-step CVD procedure, as schematically illustrated in Fig. 4a. In addition, achieving high reactivity while preserving high stability at high loadings is a huge challenge for DACs. Based on the ALD technique (Fig. 4b), Lu *et al.* solved the problem by synergizing metal–support interactions and spatial confinement, which enables the fabrication of highly loaded atomic nickel (3.1 wt%) along with dense atomic copper grippers (8.1 wt%) on a graphitic carbon nitride support (Ni$_1$Cu$_2$/g-C$_3$N$_4$).[52] Apart from heteronuclear DACs, Yan *et al.* successfully prepared a homonuclear Pt$_2$ diatomic catalyst (Pt$_2$/graphene) through a two-step ALD process.[32] Another widely used bottom-up strategy for the preparation of DACs is the wet-chemistry method. Tian *et al.* synthesized a highly dispersed Fe$_2$ diatomic catalyst loaded on mesoporous carbon nitride (mp g-C$_3$N$_4$) by an impregnation method *via* "preselection of precursors".[33]

As for top-down strategies, bulk metal or metal nanoparticles are often employed as precursors, while the metal–metal bonds are broken to generate atomically dispersed metal dimers on the substrates. Compared with bottom-up strategies, the top-down strategies could more efficiently fabricate well-defined DACs with precise structures.[53,54] Generally, high temperatures are utilized to initiate this procedure. For example, Sun *et al.* reported a new design of discrete Zn/Co bimetallic sites supported on N doped carbon (Zn/CoN–C) by a competitive complexation strategy at high-temperatures,[55] whereby chitosan was used as C and N sources and zinc chloride and cobalt acetate are selected as metal precursors (Fig. 4c). Chen *et al.* developed a bifunctional DAC consisting of high-density Ni and
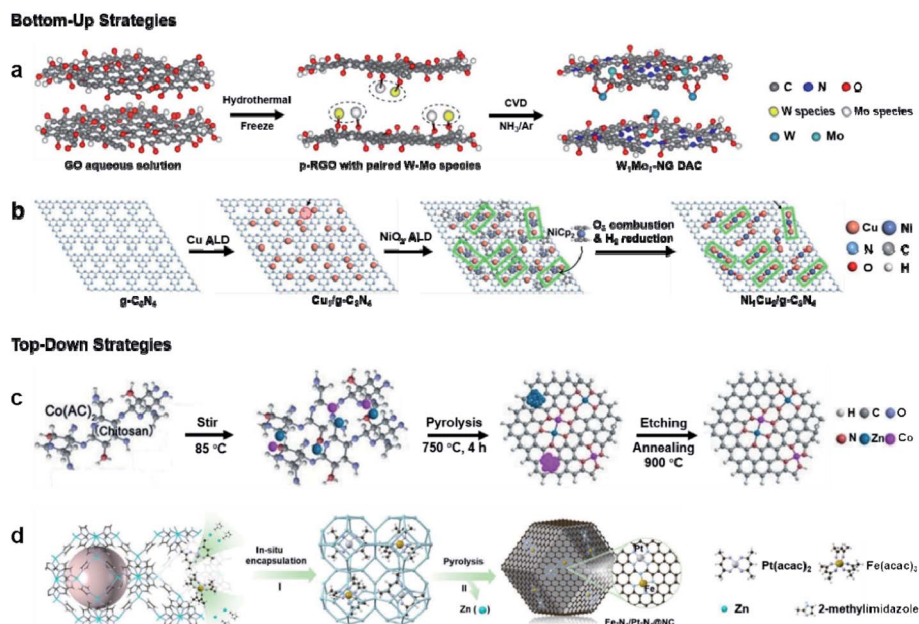
Fig. 4 (a) Schematic illustration of the synthetic procedure of W_1Mo_1–NG DAC. Reproduced from ref. 51 with permission from the authors and exclusive licensee American Association for the Advancement of Science, copyright 2020. (b) Schematic illustration of the formation of Ni_1Cu_2/g-C_3N_4 catalyst. Reproduced from ref. 52 with permission from the authors, under exclusive license to Springer Nature Limited, copyright 2021. (c) Illustration of the formation of Zn/CoN–C. Reproduced from ref. 55 with permission from Wiley-VCH GmbH, copyright 2019. (d) Synthesis process of Fe–N_4/Pt–N_4@NC. Reproduced from ref. 57 with permission from Wiley-VCH GmbH, copyright 2021.

Fe atoms anchored on N-doped graphene (NiFe-DACs) by pyrolyzing L-alanine (amino acid), ferric(II) acetate, nickel(II) acetate tetrahydrate, and melamine together in an argon atmosphere.[56] In addition, the pyrolysis of MOFs and ZIFs containing specific metal atoms is a widely used method for the synthesis of DACs anchored on carbon-based materials. For instance, Li *et al.* designed and synthesized an Fe–N_4/Pt–N_4@NC DAC through a spatial confinement strategy, as shown in Fig. 4d.[57] They employed zeolite imidazole frameworks (ZIF8s) as N-rich carbon precursors to generate exclusive M–N_4 active sites. Fu *et al.* constructed atomically dispersed Cu@N_4 and Zn@N_4 on a N-doped carbon support (Cu/Zn@NC) by directly pyrolyzing a CuZn-ZIF precursor.[58] Additionally, Xu *et al.* used a unique MOF with abundant ordered aromatic ring arrays; based on this MOF, separately loading a series of tri-nuclear complexes, they realized an effective modulation for the aggregation states of iron atoms from nanoclusters to dimers by carefully introducing a second metal ion (Zn/Co) into the Fe-complexes (Fe_2/Co_1-GNCL).[59] In all, the structure of the ordered mesoporous framework ensured the full accessibility of two kinds of homogeneously distributed single-atom sites, providing great opportunities to facilitate the reactivity with synergetic effects.

2.4 Single-atomic alloys (SAAs)

Single-atomic alloys (SAAs) are another type of atomic site catalysts, which are obtained by initiating single atoms on the surface of traditional metals.[60–62] Generally, the design of SAAs includes low amounts of components, present in the form of individual atoms, which are isolated from each other. In other words, SAAs could be described as materials formed from bi- and multi-metallic complexes, where one of these metals is atomically dispersed in another material. In contrast to the development of traditional catalysts, SAAs were first developed using single-crystal surface science and scanning probe microscopy of model samples, and this information was used in the synthesis, characterization and reactivity testing of traditional catalysts. Therefore, the development of a simple and effective method to prepare SAAs is a prerequisite for acquiring highly active catalysts. So far, some synthetic methods have been developed for the synthesis of SAAs, including sequential reduction, dealloying, galvanic replacement, wetness impregnation, and other synthetic strategies. In this section, we will not summarize all reported synthetic methods in detail, but only highlight some regularly used and newly developed methods.

Sequential reduction is a widely used technique to prepare SAAs, involving the reduction of one metal pre-cursor first, which is then used as a seed, while another metal precursor is added to the seed metal to form specific SAAs. This method can overcome the difficulty of controlling the composition and structure of catalysts in the one-pot method. For example, when the substrate is a noble metal such as Au, as shown in Fig. 5a, sequential reduction has been used effectively to deposit small amounts of dopant metals, such as Ni and Pd onto the already synthesized Au nanoparticles.[26] It was briefly described that the Au nanoparticles are firstly prepared by reducing the gold precursor, and then appropriate amounts of another metal precursor and reducing agents are added through sequential reduction, resulting in the formation of an unsupported sample
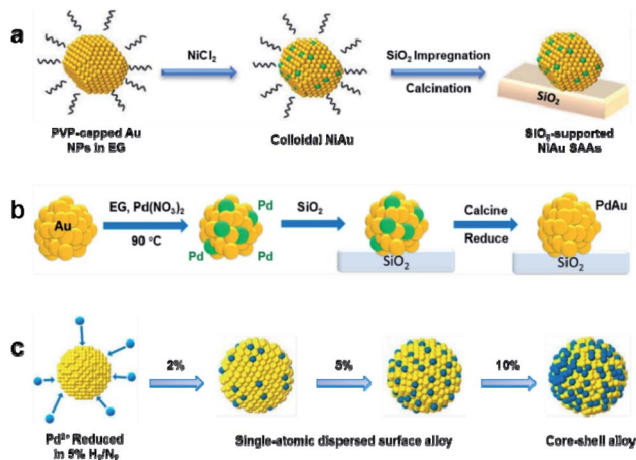
5678 | *J. Mater. Chem. A*, 2022, **10**, 5673–5698

This journal is © The Royal Society of Chemistry 2022

Fig. 5 Sequential reduction method: (a) schematic representation of the sequential reduction method for the synthesis of SiO$_2$-supported NiAu SAAs. Reproduced from ref. 26 with permission from the American Chemical Society, copyright 2020. (b) Schematic illustration of PdAu SAAs synthesis in which the final reduction step leads to migration of Pd to the interior of the NPs. Reproduced from ref. 63 with permission from the author(s), copyright 2021. (c) Illustration of the synthetic scheme for the Pd@Au SAAs with control over the dose of Pd. Reproduced from ref. 64 with permission from the American Chemical Society, copyright 2019.
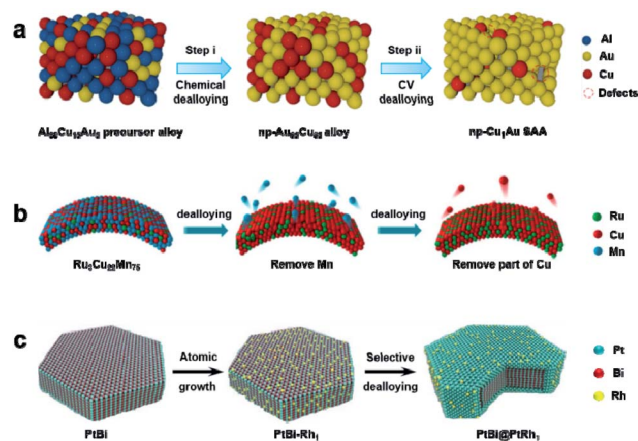

Fig. 6 Dealloying method: (a) schematic illustration for the preparation of np-Cu$_1$Au SAA with surface defects. Reproduced from ref. 65 with permission from Science China Press and Springer-Verlag GmbH Germany, copyright 2021. (b) Schematic illustration of the preparation procedure of np-Cu$_{100-x}$Ru$_x$. Reproduced from ref. 66 with permission from the American Chemical Society, copyright 2020. (c) Schematic illustration of the preparation procedure of PtBi-3.6% Rh$_1$ and PtBi@PtRh$_1$ nanoplates. Reproduced from ref. 67 with permission from Wiley-VCH GmbH, copyright 2021.

which could be supported on a substrate. The superiority of this synthetic method ensures the formation of alloys as it occurs prior to the deposition of metal particles on the support. In addition, Sykes et $al.$ synthesized and tested a kind of PdAu/SiO$_2$ bimetallic catalyst.[63] Pd$_{0.02}$Au$_{0.98}$ SAAs with a Pd/Au atomic ratio of 1/49 were prepared by a sequential reduction method and then supported on SiO$_2$ (Fig. 5b). After the calcination and reduction process removing all surface-bound species, the most thermodynamically stable state of Pd is in the bulk of the Au NPs. Recently, Mueller et $al.$ synthesized a series of Pd@Au SAAs by decorating Au nanoparticles with controlled doses of Pd,[64] resulting in the formation of bimetallic surfaces containing Pd ensembles of various sizes (Fig. 5c). In summary, when the sequential reduction method is used to fabricate SAAs, a small amount of guest metal atoms is usually introduced in the host metal to obtain various types of SAAs. Moreover, the selection and introduction of the support is also particularly important for the preparation of SAAs.

Another commonly used method for the synthesis of SAAs is selective dealloying, which can stabilize isolated metal atoms on the surface of another host metal. For instance, Tan et $al.$ proposed a facile route to prepare atomic Cu dispersed on hierarchically nanoporous gold architectures (denoted as np-Cu$_1$Au SAAs) through a dealloying method,[65] and the fabrication process is illustrated in Fig. 6a. Firstly, the Al$_{80}$Cu$_{15}$Au$_5$ precursor alloy was designed. After the first dealloying step in NaOH solution, the α-Al phase was selectively etched and a small percentage of Al existed in the intermetallic phase, resulting in np-Al$_{13}$Cu$_{64}$Au$_{23}$. Then, nanoporous Au$_{65}$Cu$_{35}$ alloy was prepared by dealloying the as-prepared Al$_{13}$Cu$_{64}$Au$_{23}$ alloy. Recently, they also prepared a nanoporous binary Cu–Ru alloy

through dealloying a single-phase ternary Ru$_3$Cu$_{22}$Mn$_{75}$ precursor in (NH$_4$)$_2$SO$_4$ solution to remove Mn, as shown in Fig. 6b.[66] In addition, Hensen and Quan et $al.$ presented a tensile-strained Pt–Rh single-atom alloy (PtBi@PtRh$_1$ SAAs) by an electrochemical dealloying strategy.[67] Fig. 6c illustrates the design and synthesis of PtBi–Rh$_1$ and PtBi@PtRh$_1$ based on PtBi nanoplates. At a relatively high potential, electrochemical dealloying of Bi atoms was performed in acidic electrolytes. Then, Pt layers are formed due to the removal of Bi atoms from the PtBi lattices, which prevents the continuous etching of inner Bi atoms and leads to the emergence of the PtBi core–Pt shell structure. Therefore, the planting of isolated-Rh-atoms on tensile-strained Pt shells could be achieved by electrochemical dealloying.

In addition to the above major synthetic methods, other innovative strategies for the preparation of SAAs have also been proposed. For instance, Bok et $al.$ utilized the interaction between metals and MOFs to synthesize atomically dispersed Au on tensile-strained Pd nanoparticles (M–AuPd).[68] As shown in Fig. 7a, Pd and Au ions were firstly impregnated inside the pore structure of MOF-808, where confined growth was initiated under reducing conditions, then M–AuPd was obtained after etching Zr-MOF-808. In addition, galvanic replacement has been exploited to fabricate SAAs and it gained importance due to the fact that no external electricity is need for the displacement. Instead, it uses the half-reduction potential of the metal precursor. As illustrated in Fig. 7b, the reduced surface of the host metal (Cu) acts as a template to deposit the minority metal (Pd) precursor by metal exchange. As dopant metal ions are reduced, the oxidized atoms of the host metal surface start to dissolve.[26] In all, the sequential reduction contains a two-step metal precursor reduction, in which one metal atom is used as the seed. An advantage of the technique is ensuring the
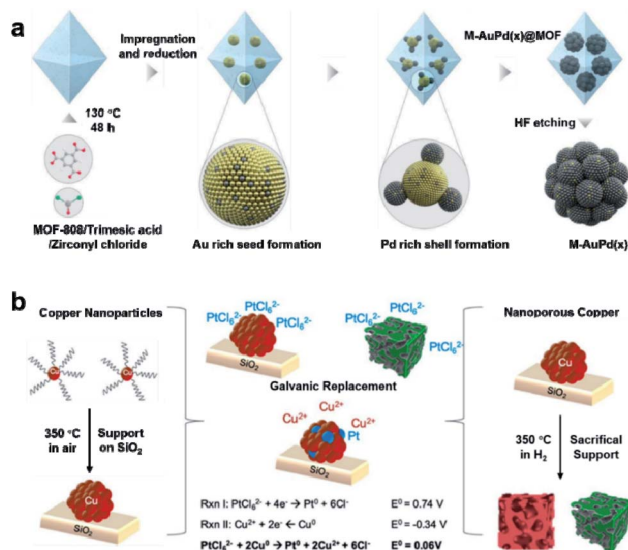
Fig. 7 Other synthetic methods: (a) synthetic scheme of the impregnation and reduction method for the synthesis of M−AuPd(*x*) catalysts. Reproduced from ref. 68 with permission from the American Chemical Society, copyright 2021. (b) Schematic representation of the galvanic replacement method for the synthesis of nanoparticle and nanoporous SAA catalysts. Reproduced from ref. 26 with permission from the American Chemical Society, copyright 2020.

formation of the alloy, because it occurs prior to deposition of metal particles on the support. Dealloying can disperse isolated metal atoms on the surface of another host metal without destroying the original metal structure. Impregnation is another simple and one-pot technique used to make bimetallic alloys. During reduction, metal precursors are mixed in solution and an appropriate amount is optimized to fill the pores of the support. Galvanic replacement is suitable to synthesize surface alloys by utilizing the semi-reduction potential of metal precursors, and it is of great interest due to its simplicity and the fact that no external electricity is required for the

displacement. The successful construction of dual-site SAAs not only expands the class of SACs, but also provides new inspiration to design and prepare high-performance catalysts at the atomic scale.

3. Characterization techniques

The identification and confirmation of the electronic, geometric configuration, and coordination environment of atomic-coupling sites at the atomic level is the prerequisite to explore the composition–structure–activity relationship of SAC-NPs, SACCs, DACs and SAAs. This is beneficial for precisely designing and tuning atomic sites towards specific catalytic reactions. However, due to the non-crystallographic ordering of single metal atoms and complex coordination structures, it is extremely challenging to fully characterize these synergistically enhanced structures. To date, various advanced and effective characterization techniques, mainly microscopic and spectroscopic methods, such as HAADF-STEM, XAS, XPS, XRD, IR and Raman spectroscopy, Mössbauer spectroscopy, nuclear magnetic resonance (NMR), and density functional theory (DFT) calculation, have already been adopted (Fig. 8).[69,70] However, each characterization technique has its own advantages and limitations. Definitive structural characterization of atomic sites requires combinations of techniques. Moreover, the structural information obtained from any characterization tool should be better verified by other techniques. Generally, HAADF-STEM is used for imaging individual metal atoms and defining the degree of uniformity of the surface species,[71,72] and electron energy loss spectroscopy (EELS) coupled with AC HAADF-STEM was even utilized to reveal the composition of single active sites. Nevertheless, their atomic resolutions are limited by magnetic lens aberration, and it's difficult to distinguish DACs containing two different metal elements with similar molecular weights due to their close brightness levels in AC HAADF-STEM images.[73] XAS is adopted to confirm metal coordination environments and provide information about
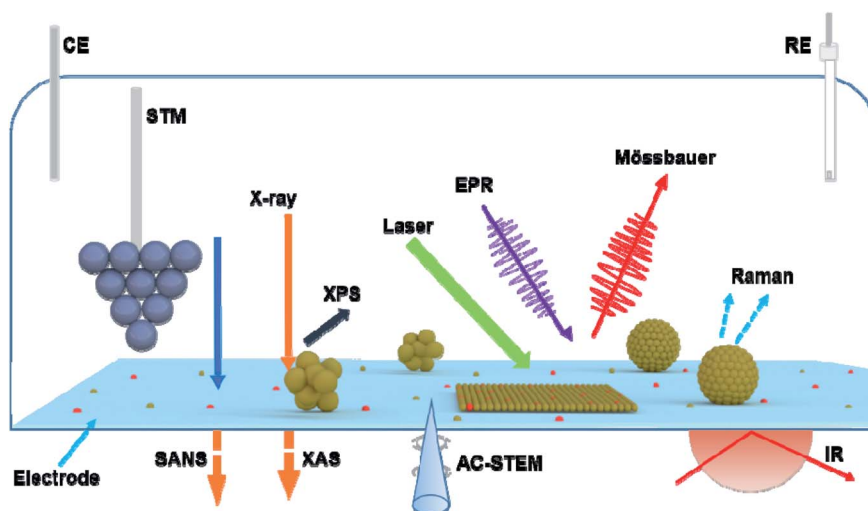

Fig. 8 Schematic illustration of characterization techniques for SACs, SAC-NPs, SACCs, DACs and SAAs.

5680 | *J. Mater. Chem. A*, 2022, **10**, 5673–5698

This journal is © The Royal Society of Chemistry 2022

oxidation valence, which is generally accepted as a key technique to gain average structural and electronic information at the atomic scale, including bond distance and coordination number.[74] It is worth mentioning that *ex situ* XAS cannot be used to monitor the dynamic evolution and modification of the oxidation state and coordination environment of active centers during the reaction, while *in situ/operando* XAS can facilitate an in-depth understanding of the catalytic mechanisms under the operating conditions.[75] XPS is another common technique to probe sample averaged information about the oxidation state of metal species at the ensemble scale, but it cannot directly detect the specific binding site of metal atoms and obtain details about the different configurations.[76] IR and Raman spectroscopies are utilized to characterize metal ligand bonds, and detect the binding of reactants and intermediates under *operando* conditions.[77] Moreover, the lack of H_2O signal makes Raman spectroscopy an ideal tool to probe the electrocatalytic mechanism of SACs in aqueous solutions. NMR and EPR spectroscopies are exploited to characterize the organic ligands of metal complexes, and determine the chemical coordination and oxidation state of various elements.[78] However, their use is restricted. NMR is applied to characterize SACs with high loadings, and EPR is only applicable to paramagnetic materials. DFT calculation always works in close collaboration with experiments, and can be used to explore the electronic structures and reaction mechanisms.[79] In this section, we will briefly highlight important features of different characterization techniques to acquire the coordination environment information of SAC-NPs, SACCs, DACs and SAAs.

3.1 AC HAADF-STEM

Aberration-corrected high-angle annular dark-field scanning transmission electron microscopy (AC HAADF-STEM) is a powerful tool to characterize the morphology and structure of atomically dispersed catalysts. STEM instruments can achieve an electron probe with a sub-Ångstrom size, and these electrons are scattered and collected using a high angle HAADF detector, which is capable of obtaining atomic resolution images due to the introduction of aberration correctors.[80–82] Generally, when the atomic numbers of metal atoms are much higher than those of support atoms, AC HAADF-STEM can provide a visual observation of the position and distribution of single-atomic structures on substrates. In addition to spatial distribution, this technique is also used to analyze crystallization information related to the surface structure of substrates.[83] More importantly, the local coordination environment of single atoms can also be directly distinguished by AC HAADF-STEM, which provides adequate information to build a theoretical model. For example, Spendelow and Wu *et al.* observed that Pt NPs with a uniform particle size of about 2.4 nm co-exist with FeN_4 sites embedded in carbon (Fig. 9a and b), this is a typical feature of SAC-NP catalysts.[37] In addition to nanoparticles, clusters can also be clearly observed by STEM. Cheng *et al.* constructed a Ru atomically dispersed catalyst (Ru ADC) with Ru–C_5 single atoms
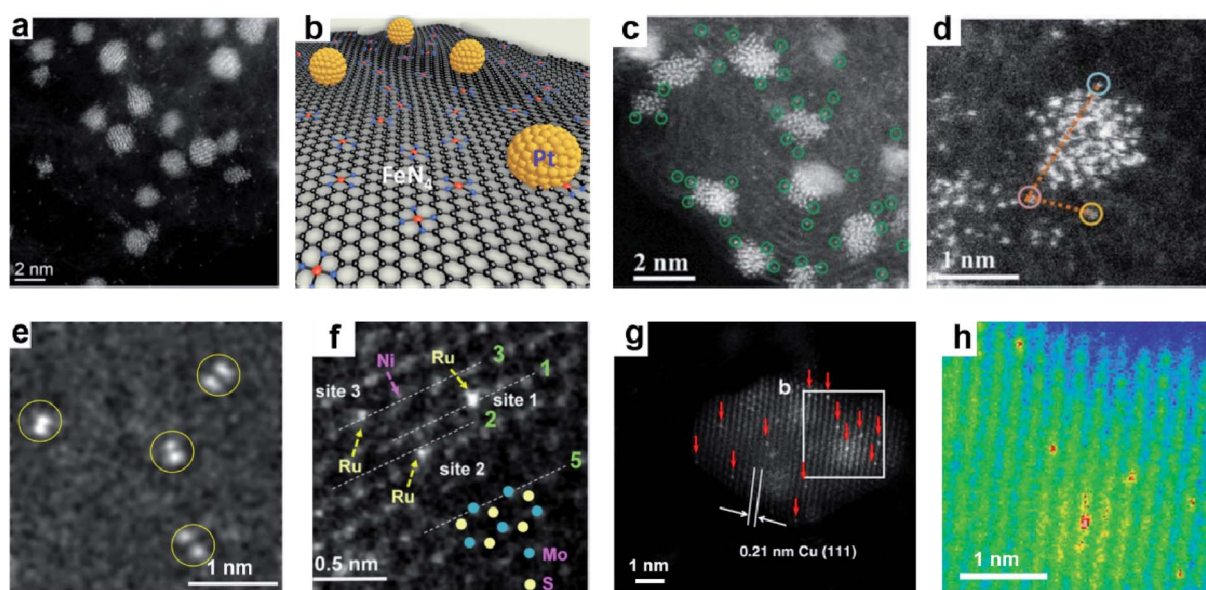

Fig. 9 AC HAADF-STEM: (a) STEM images of the Pt/FeN$_4$−C catalyst showing a uniform distribution of Pt nanoparticles and the coexistence with FeN$_4$ sites. (b) Schematics of Pt/FeN$_4$−C (Pt−Co/FeN$_4$−C) catalysts. Reproduced from ref. 37 with permission from the Royal Society of Chemistry, copyright 2021. (c and d) AC-STEM image and the corresponding extracted line profiles of Ru ADC. Reproduced from ref. 34 with permission from Wiley-VCH GmbH, copyright 2021. (e) Aberration-corrected HAADF-STEM images of dimeric Pt$_2$/graphene, dimers are highlighted with yellow circles. Reproduced from ref. 32 with permission from the author(s), copyright 2017. (f) The HAADF-STEM image of Ru/Ni−MoS$_2$. Reproduced from ref. 84 with permission from Elsevier B.V., copyright 2021. (g) HAADF-STEM images with the typical region of the reduced 0.1Pt$_{10}$Cu/Al$_2$O$_3$ catalyst, showing Pt atoms individually dispersed on Cu(111). Pt atoms are highlighted with red arrows. (h) The colored intensity map from the selected region in (i). The lattice spacing of Pt/Cu SAA is 0.21 nm, which is consistent with that of Cu(111). Reproduced from ref. 85 with permission from the author(s), copyright 2018.

This journal is © The Royal Society of Chemistry 2022

J. Mater. Chem. A, 2022, **10**, 5673–5698 | **5681**

and Ru oxide nanoclusters (~1.5 nm).[34] AC HAADF-STEM was used to obtain atomic resolution information of Ru ADC. As shown in Fig. 9c and d, atomically dispersed nanoclusters and abundant single atoms can be obviously observed on the support at the same time. Compared with coexisting nanoparticles and clusters, it is much more difficult to characterize diatoms. For example, Lu *et al.* noticed that Pt_2 dimers frequently rotated about specified angles of 30, 60, and 90° under an electron beam during STEM measurements and then split into two isolated Pt_1 atoms (Fig. 9e).[32] Lei *et al.* fabricated a dimetallic single-atom catalyst where monoatomic Ru and Ni co-modify MoS_2 (Ru/Ni–MoS_2).[84] From the HAADF-STEM image (Fig. 9f), we can see clearly that the single Ni atoms occupy the positions of the Mo atoms in the MoS_2 plane. On the other hand, when the atomic numbers of metal atoms are close to those of support atoms, it is more difficult to distinguish these atomically dispersed metal sites. Gong *et al.* synthesized an

alumina-supported Pt/Cu SAA catalyst, and the structure of Pt/Cu SAAs was characterized by AC HAADF-STEM images.[85] From Fig. 9g and h, single Pt atoms could be distinguished from Cu atoms due to differences in the Z-contrast, indicating the presence of individual brighter Pt atoms amidst Cu nanoparticles. Additionally, active sites with atomic numbers less than those of support elements can also be identified by STEM images, providing a technical base for further analysis of SAC-NPs, SACCs, DACs and SAAs.

3.2 X-ray absorption spectroscopy (XAS)

X-ray absorption spectroscopy (XAS) based on synchrotron radiation is another powerful technology to characterize atomically dispersed catalysts and determine the geometric and electronic structure state of SAC-NPs, SACCs, DACs and SAAs, which could be divided into X-ray absorption near edge structure (XANES) and extended X-ray absorption fine structure

Fig. 10 XAS: (a) schematic illustration of the basic principle and typical spectrum of XAS. Reproduced from ref. 53 with permission from the American Chemical Society, copyright 2020. (b) Co K-edge XANES spectrum of CNT@SAC-Co/NCP, CoPc, Co foil, and CoO. (c) Fourier-transform EXAFS spectrum of CNT@SAC-Co/NCP, CoPc and Co foil. Reproduced from ref. 88 with permission from Wiley-VCH GmbH, copyright 2021. (d) XANES spectra (inset: model of $Fe_{AC}@Fe_{SA}$–N–C. Fe red, N blue, C gray spheres) and (e) FT-EXAFS curves of $Fe_{AC}@Fe_{SA}$–N–C, Fe_{SA}–N–C, and reference materials at the Fe K-edge. Reproduced from ref. 47 with permission from the American Chemical Society, copyright 2019. (f) EXAFS fitting curves of Ni K-edge in Ru/Ni–MoS_2 (inset: atomic structure model of Ru/Ni–MoS_2). Reproduced from ref. 84 with permission from Elsevier B.V., copyright 2021. (g) Left: the K2-weighted Fourier transform spectra of MeCpPtMe/graphene, Pt_1/graphene, and Pt_2/graphene at the Pt L3-edge. The reference samples of Pt foil, PtO_2, and $MeCpPtMe_3$ are also shown for comparison. Right: comparison of the EXAFS simulations based on the corresponding DFT calculated structural models (insets) with the experimental EXAFS spectra of Pt_1/graphene and Pt_2/graphene. The balls in gray, white, red, and dark blue represent carbon, hydrogen, oxygen, and platinum, respectively. Reproduced from ref. 32 with permission from the author(s), copyright 2019. (h) *In situ* Fourier transform EXAFS spectra of the xPd-Ni/SiO_2 samples (x = 5, 10, and 20) and Pd foil reference in the real space at the Pd K-edge. Reproduced from ref. 89 with permission from the author(s), copyright 2019.

5682 | *J. Mater. Chem. A*, 2022, **10**, 5673–5698

This journal is © The Royal Society of Chemistry 2022

(EXAFS) according to the relative energy to the absorption edge of the specific element (Fig. 10a).[53] Generally, XANES rises sharply and oscillates strongly near the absorption edge, while EXAFS is the weak oscillatory wiggles above the absorption edge about 50 eV. Compared with EXAFS, XANES is more complicated due to the multiple scattering characteristic and polarization effect. Moreover, the coordination environment of target atoms, such as bond distance, electronic orbits, valence states and coordination number, could be qualitatively evaluated by the Fourier transform (FT) and wavelet transform (WT) of EXAFS. In addition, XANES generally focuses on the characteristic peak, oxidation state and theoretical analysis. Therefore, XANES contributes to the clarification of the interaction between atomic sites and supports, and provides reliable theoretical structure models.[86,87]

Of course, we should also be aware that the structural information obtained by XAS is an average result of the detected element if different coordination structures exist in SAC-NPs, SACCs, DACs and SAAs. For example, Shao *et al.* synthesized a dual-phasic carbon bifunctional electrocatalyst. Specifically, a cobalt single-atomic catalyst supported on carbon nanotubes (single-atom phase) and Co nanoparticles encapsulated in a ZIF-derived carbon polyhedron (nanosized phase) are integrated together through carbon nanotube bridges (CNT@SAC-Co/NCP).[88] XAS was applied to understand the structure of the catalyst deeply, Fig. 10b shows the Co K-edge near-edge structure (XANES) spectrum. The absorption edge position is between those of standard Co foil and CoO/cobalt phthalocyanine (CoPc), implying the coexistence of 0 and +2 valence states of Co in the CNT@SAC-Co/NCP. The Fourier-transform extended X-ray absorption fine structure (FT-EXAFS) spectrum in Fig. 10c shows a Co–N scattering peak at 1.5 Å and Co–Co scattering peak at 2.2 Å, further revealing that CNT@SAC-Co/NCP is composed of Co single-atomic and nanosized Co phase. Similarly, Ao *et al.* fabricated an electrocatalyst in which atom clusters are embedded in an atomically dispersed Fe–N–C matrix ($Fe_{AC}@Fe_{SA}$–N–C).[47] To understand and compare the electronic structure and local atomic coordination of $Fe_{AC}@Fe_{SA}$–N–C and Fe_{SA}–N–C, XANES and EXAFS were performed. As shown in Fig. 10d and e, the near-edge absorption threshold of the Fe K-edge of Fe_{SA}–N–C was similar to that of FePc, indicating that the single Fe atoms carried positive charges and are coordinated by N atoms. The FT-EXAFS spectra of both $Fe_{AC}@Fe_{SA}$–N–C and Fe_{SA}–N–C show a primary peak located at ~1.5 Å, corresponding to the Fe–N(O) scattering path. Additionally, Lei *et al.* fabricated a dimetallic single-atom catalyst in which monoatomic Ru and Ni co-modify MoS_2 ($Ru/Ni–MoS_2$).[84] The EXAFS fitting demonstrates that the coordination numbers and bond-lengths of Ni atoms in $Ni–MoS_2$ are nearly identical to Mo in MoS_2 (Fig. 10f), which proves that Ni atoms substituted Mo in the MoS_2 lattice by isomorphous substitution. XAS also presents unique advantages for more complex diatomic systems. For instance, XAFS spectra and DFT calculations suggest that the Pt_2 dimers are likely in the oxidized form in Pt_2O_x. As shown in Fig. 10g, the dimeric Pt_2/graphene sample showed a similar FT curve to Pt_1/graphene, indicating a similar local C/O coordination.[32] Moreover, in the Pt_2/graphene spectrum, there was no

visible peak for the Pt–Pt coordination, suggesting the Pt_2 dimers are in the oxidized state. Lu *et al.* also adopted XAS to establish the structure–activity relationship of PdNi SAAs.[89] EXAFS curve fittings revealed that Pd–Ni coordination is the dominant one with a coordination number of 5.5, while Pd–Pd coordination has a minor contribution with a CN of only 1.2 (Fig. 10h), suggesting that Pd atoms are atomically dispersed in majority. To summarize, the XAS technique consisting of both EXAFS and XANES provides convincing structural information on SAC-NPs, SACCs, DACs and SAAs, and is regarded as the most powerful tool to obtain the local electronic structure and environmental coordination information.

3.3 Other applicable characterization techniques

Besides AC-STEM and XAS techniques, other methods, such as Mössbauer spectroscopy, scanning tunneling microscopy (STM), electron paramagnetic resonance (EPR) spectroscopy, IR spectroscopy, and DFT calculation can be applied to characterize single-atomic synergistic sites. Specifically, Mössbauer spectroscopy is a powerful technique based on the Mössbauer effect to investigate the chemical environment, coordination structure, and spin state of Mössbauer active elements *via* measuring the hyperfine interactions caused by the electric and magnetic fields acting on an atomic nucleus, and is especially suitable for Fe SACs.[90] For example, Li *et al.* constructed an electrocatalyst with Fe–Co dual sites embedded on N-doped porous carbon. In the Mössbauer spectrum of Fe–Co DACs, apart from the typical signal of three doublets, a minor amount of singlet component occurs.[91] This extra peak could be attributed to the Fe–Co bond, which provides direct evidence for the formation of dual sites. In addition, the STM is an effective characterization technique to directly observe and pinpoint the atomic sites by the needle tip and atomic-resolution microscopic images. Moreover, it could be utilized to accurately detect the electronic structure information of metal sites.[92,93] In a typical STM experiment designed to characterize atomic-coupling sites, firstly, adsorbed atoms are deposited on single-crystal substrates in UHV by evaporation, and then are imaged by quantifying the current passing through an atomically sharp probe tip. Additionally, IR spectroscopy is also a valuable technique to characterize supported metal pair-sites through supplying fingerprint information of their ligands on the metals or metal–support interactions and metal nuclearities.[94,95] This method not only detects the binding of reactants and intermediates under *in situ* or *operando* conditions but also provides electronic and geometric information on the metal centers. Moreover, the dynamic variation of the coordination state in catalytic centers during reactions could also be distinguished by the vibrational frequency of probe molecules. Similarly, in terms of atomic-scale structural and electronic properties, electron paramagnetic resonance (EPR) spectroscopy is another promising technique to probe the unpaired electron spin effect, chemical coordination and oxidation state of single active sites in SACs, SAC-NPs, SACCs, DACs and SAAs.[96] However, EPR is only applicable to paramagnetic species. For example, Jiang *et al.* designed an atomically dispersed Co deposit onto the

This journal is © The Royal Society of Chemistry 2022

J. Mater. Chem. A, 2022, **10**, 5673–5698 | **5683**

surface of Ru tiny sub-nanoclusters (Co$_1$Ru TCs).[43] According to the EPR spectra, the *g* value (2.56) of Co$_1$Ru TCs could be ascribed to the unpaired electron in the orbital of Co^{II} and Ru^{III}. To explore the effect of electronic interaction between the atomically dispersed Co and Ru clusters, dual atomically dispersed Co and Ru (denoted as Co$_1$Ru DAs) were also prepared. In comparison with Co$_1$Ru DAs (*g* = 2.19), the increase in the *g* value of Co$_1$Ru TCs is due to the influence of spin–spin strain interaction between subnano Ru clusters and single Co atoms. This shows the practicality of EPR for single-atomic site resolution. The density functional theory method has been developed in parallel with experiments, and is currently indispensable for the studies of SACs, DACs and SAAs. On one hand, DFT calculations could explain and obtain charge distribution, adsorption energies and reaction mechanism. On the other hand, they could be exploited to predict and rationally design efficient synergistic catalysts. For example, based on DFT calculations, Lu *et al.* found that the unoccupied 5d state of Pt atoms in Pt$_2$/graphene shows a noticeably higher energy position of 0.87 eV than that of the Pt atom in Pt$_1$/graphene (0.40 eV), indicating that Pt$_1$/graphene is more prone to accepting electrons than Pt$_2$/graphene, which shows stronger CO adsorption on Pt$_1$.[32]

4.   Applications in electrocatalysis

With increasing attention to severe environmental problems and shortage of fossil fuels, the development of sustainable and clean electrochemical conversion to produce valuable fuels and chemicals has become particularly significant.[97–99] Electrocatalysis reaction (CO$_2$RR, ORR, HER, OER and N$_2$RR *etc.*) lies at the center of clean energy conversion due to the mild reaction conditions and excellent compatibility. Furthermore, catalysts are an indispensable part of catalytic systems, and rational designs of highly efficient and durable electrocatalysts play a key role in improving the reactivity and selectivity, but face huge challenges at the same time.[100] Over the past few years, SACs have achieved great success in the electrocatalytic field due to their unique structural and electronic properties. On one hand, the catalytic activity and rates could be greatly improved by engineering the structure and coordination environment of the SACs. On the other hand, SACs have a well-defined active site structure, which helps to clarify the relationship between material structure and activity at the atomic level.[101,102]

Recently, some researchers have paid attention to the dynamic evaluation of single-atomic sites in electrochemistry systems. The changes of coordination number (CN), atom type, valence state, and synergistic structure of SACs have a great effect on the reactivity and selectivity. For example, to elucidate the origin of the excellent CO$_2$RR activity of atomically dispersed Fe–N–C catalysts, based on *operando* ^{57}Fe Mössbauer spectroscopy, Liu *et al.* found that the *in situ*-generated four pyrrolic nitrogen-coordinated low-spin Fe(I) (LS Fe^{I}N$_4$) featuring monovalent iron is identified as the real active center for the conversion of CO$_2$ to CO.[103] Besides, Zeng *et al.* demonstrated that a single-atom iron catalyst with *in situ* generated Fe^{4+} centers is highly active toward the OER. Experimental and

theoretical studies revealed that the valence state of the metal center changed from Fe^{3+} to the highly active Fe^{4+} prior to the OER process.[104] Wei *et al.* directly observed that one oxygen atom is formed at the Ir active site with an O-hetero-Ir–N$_4$ structure as a more electrophilic active centre for the OER in an acidic medium by using *in situ* X-ray absorption spectroscopy.[105] Therefore, the dynamic evaluation of single atoms during the reaction process is crucial to elucidate the real synergistic effect and reaction mechanism.

Generally, different active sites could make these materials work as multi-functional catalysts. Unlike SACs, the biggest advantage of synergistically enhanced single-atom sites is the interaction between adjacent metal atoms. The interaction between two metal sites in SAC-NPs, SACCs, DACs and SAAs is helpful to precisely adjust the dual-atomic configuration and generate synergetic effects. For example, in DACs, two adjacent metal atoms are bonded to each other, which mainly promotes the activity by regulating the binding energy of reaction intermediates.[106,107] DACs can be further classified into two categories: (i) homo-paired DACs with identical metal atoms, and (ii) hetero-paired DACs with different metal atoms, which could be applied to various electrocatalytic reactions. In addition, compared to monoatomic catalysts, the interaction of atoms will be more complicated in SAC-NPs, SACCs, DACs and SAAs, including the overlapping of orbitals and electronic structure change, which depends on the number of atoms, nuclear nature, and synergistic effect. According to the Sabatier principle, the binding strength of reactants, intermediates and products on an excellent catalyst should be moderate, neither too weak to activate the reactants nor too strong to poison the active sites, which could be attributed to the existence of scaling properties of adsorption energies on the metal surface.[2,108,109] The unique geometry and electronic structure of synergistic sites could adjust the energy barrier of activation, which in turn affects the reactivity and meeting specific reaction requirements. In this section, some representative catalytic reactions are selected to illustrate the unique structure–property relationship of SAC-NPs, SACCs, DACs and SAAs.

4.1   Synergistic single-atomic catalysis in the CO$_2$RR

The electrochemical reduction of carbon dioxide (CO$_2$RR) to value-added fuels or chemicals (*i.e.*, carbon monoxide, formate, methanol, methane, ethylene, ethanol, *etc.*) provides a promising route to alleviate global carbon balance and energy crisis. A high overpotential is needed to overcome the activation barrier of CO$_2$ reduction, but the high reduction potential will also cause the violent competition reaction of the HER, which greatly reduces the faradaic efficiency and selectivity of the CO$_2$RR.[110,111] Thus, the exploitation of an active and stable electrocatalyst is highly demanded. In addition, the scaling relationships between the adsorption strength of reaction intermediates (such as *CO, *COOH, *CHO) strongly restrict the theoretical performance.[112] The CO$_2$RR involves multi-proton-coupled electron transfer (PCET) and a complex reduction mechanism, which further limit the catalytic activity, while the synergistic effect and more sophisticated functionalities in

5684 | *J. Mater. Chem. A*, 2022, **10**, 5673–5698

This journal is © The Royal Society of Chemistry 2022

SAC-NPs, SACCs, DACs and SAAs may overcome this limitation, where two catalytic sites can provide different intermediate binding energies to break scaling relationships and achieve excellent CO_2RR activity, as summarized in Table 1. Moreover, the reaction kinetics could be boosted by the atomic dispersion sites. For example, a single-atom incorporated carbon material is an effective CO_2RR catalyst due to the strong interaction between metal atoms and substrates, but the carbon-based SACs still cannot solve the issue of slow reaction kinetics.[113] Based on this, Ye et al. developed a sheet-like open nanostructure with a metal Ni core wrapped by a Ni–N doped carbon skeleton (Ni-NC@Ni). Such a nanostructure mainly presents

Table 1 A summary of synergistic single-atomic catalysis in the CO_2RR

Synergistic effect	Catalysts	Performance or parameters	Ref.
SAC-NPs	Ni-NC@Ni	High selectivity for CO product (faradaic efficiency ~87%) at a moderate overpotential of 670 mV	Nano Energy, 2020, **77**, 105010 (ref. 38)
SAC-NPs	Ni@NiN$_4$CM	The maximum CO$_{FE}$ of around 97.6% at −0.9 V and >90% CO selectivity at a high current density of 100 mA cm^{-2}	Angew. Chem., Int. Ed., 2021, **60**, 11959 (ref. 39)
SACCs	Cu–S$_1$N$_3$/Cu$_x$	High FE$_{CO}$ over 90% from −0.55 to −0.75 V, outperforming the analogues with Cu–N$_4$ (~54%) and Cu–S$_1$N$_3$ (70%)	Angew. Chem., Int. Ed.,2021,**60**, 24022, DOI: (ref. 114)
SACCs	Au$_{19}$Cd$_2$	Exhibits the highest CO_2RR activity (2200 mA mg^{-1} at −1.0 V vs. RHE) among the reported gold nanoclusters	Angew. Chem., Int. Ed., 2021, **60**, 6351 (ref. 145)
DACs	Pd$_2$ DAC	With 98.2% CO faradaic efficiency at −0.85 V vs. RHE, far exceeding that of Pd$_1$ SAC	Angew. Chem., Int. Ed., 2021, **60**, 13388 (ref. 117)
DACs	Ni$_2$/NC	The dinuclear Ni$_2$ catalyst exhibits >94% faradaic efficiency for efficient carbon monoxide production	J. Am. Chem. Soc., 2021, **143**, 11317 (ref. 116)
DACs	CoNi-NC	Show a high syngas evolution (total current > 74 mA cm^{-2}) with CO/H$_2$ ratios (0.23–2.26)	Angew. Chem., Int. Ed., 2020, **59**, 3033 (ref. 146)
DACs	ZnCoNC	Show a CO faradaic efficiency of 93.2% at −0.5 V vs. RHE during a 30 hours test	Angew. Chem., Int. Ed., 2020, **59**, 12664 (ref. 118)
DACs	Ni/Fe–N–C	Exhibits high selectivity with CO faradaic efficiency above 90% over a wide potential range from −0.5 to −0.9 V	Angew. Chem., Int. Ed., 2019, **58**, 6972 (ref. 147)
DACs	Fe/Cu–N–C	Exhibits an excellent CO faradaic efficiency >95% over a wide potential range of −0.4 to −1.1 V vs. RHE	J. Mater. Chem. A, 2021, **9**, 23817, DOI: (ref. 115)
SAAs	np-Cu$_1$Au SAA	With nearly 100% CO Faraday efficiency in a wide potential range (−0.4 to −0.9 V vs. RHE	Sci. China. Mater., 2021, **64**, 1900 (ref. 65)
SAAs	Bi–Pd SAA NDs	The FEs of CO reach 91.8% in gas diffusion flow cells with overpotentials of only 200 mV	Appl. Catal. B: Environ., 2021, **289**, 119783 (ref. 121)
SAAs	M–AuPd(20)	M–AuPd showed 26-fold enhancement in partial current density toward formate with >99% FE, compared to Pd/C	J. Am. Chem. Soc., 2021, **143**, 5386 (ref. 68)
SAAs	Pd@Au	Catalytic activity for electroreduction of CO_2 to CO exhibits a nonlinear behavior depending on the Pd content	J. Am. Chem. Soc., 2019, **141**, 16635 (ref. 64)
SAAs	Cu$_1$Sn$_1$	A maximum faradaic efficiency (FE) of 95.4% for formate at −1.2 V vs. RHE	ACS Catal., 2021, **11**, 11103 (ref. 148)

This journal is © The Royal Society of Chemistry 2022

J. Mater. Chem. A, 2022, **10**, 5673–5698 | **5685**

two major advantages: (i) the rich isolated Ni–N species (~4.23 at%) embedded in the carbon layer acts as an active site for the CO_2RR to produce CO; (ii) the Ni nanoparticle core wrapped by the carbon shell serves as a good conductor to accelerate electron transport.[38] Owing to these structural properties, the Ni–NC@Ni catalyst exhibits excellent CO_2RR activity.

In addition, it has been proved that the transfer of the delocalized unpaired electron from the TM center to reactants was beneficial for the activation and adsorption of CO_2 molecules. By introducing TM nanoparticles (NPs) in a single-atom catalytic system, the formation of adsorbed hydrogen with a suitable binding energy to accelerate the protonation reaction kinetics could be promoted. For example, Hou *et al.* developed a hybrid CO_2RR catalyst containing Ni NPs supported by a carbon matrix with atomically dispersed NiN sites (Ni@NiNCM). As shown in Fig. 11a, the Ni@NiNCM catalyst delivered more favorable CO_2RR activity than the NiNCM catalyst.[39] The computational studies also predicted that the Ni NPs could modify the electronic structures of adjacent NiN_4 centers to form an interactive active center, which could accelerate the *COOH transition to *CO by virtue of the short bond length

(Fig. 11b and c). In addition to TM nanoparticles, nanoclusters are also introduced to enhance the reactivity. Yu *et al.* designed a novel tandem electrocatalyst for CO_2-to-CO conversion comprising a single Cu site and dispersed Cu clusters, denoted as $Cu–S_1N_3/Cu_x$. The experimental results show that the adjacent Cu_x cluster sites could effectively promote the protonation of $*CO_2^-$ by accelerating water dissociation and offering *H to $Cu–S_1N_3$ active sites.[114] Additionally, as another further expansion of the SAC series, DACs introduce synergistic sites to distribute electrons, which can break the linear relationship of adsorption energies of different reaction intermediates. For instance, an Fe–Cu diatomic site with a unique coordination structure ($FeN_4–CuN_3$) was precisely controlled by He *et al.*[115] As shown in Fig. 11d, compared to $Cu–N_4$ and $Fe–N_4$, $FeN_4–CuN_3$ has a more positive $U_L(CO_2) - U_L(H_2)$ value, confirming its ability to restrict the HER and promote CO production. Yao *et al.* designed a uniform atomically precise Ni_2 site, consisting of two $Ni_1–N_4$ moieties on a nitrogen-doped carbon (Ni_2/NC).[116] According to the Gibbs free energy diagram and reaction pathways (Fig. 11e), the $O–Ni_2–N_6$, $Ni_2–N_6$, $Ni–N_4$, and N-G models displayed free energy changes (ΔG) of 0.77, 1.35, 1.54,
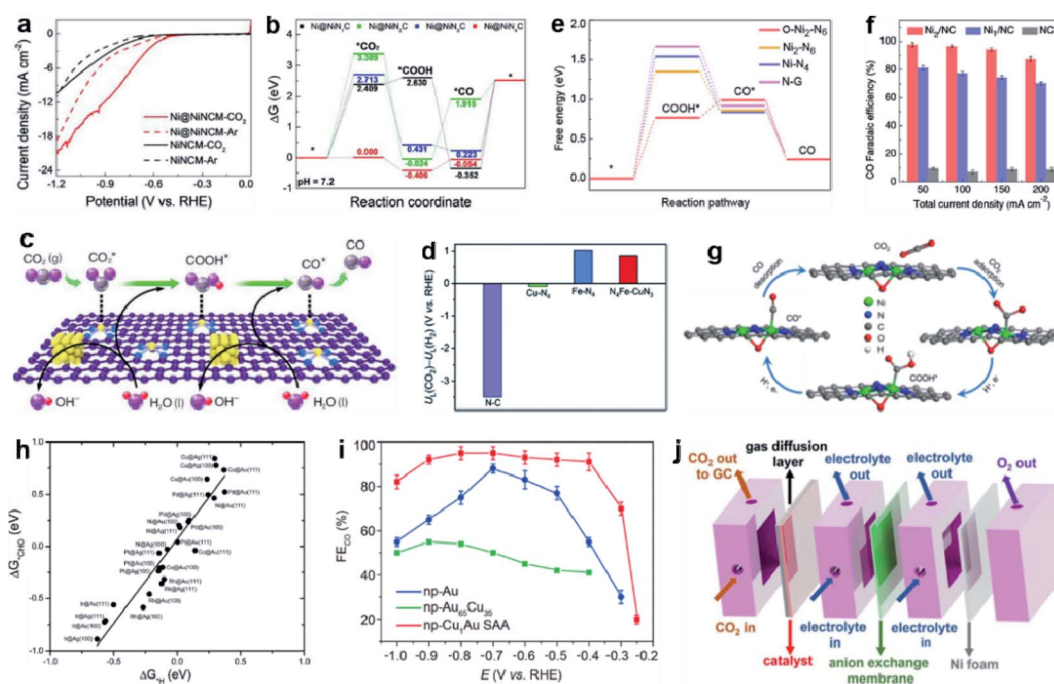

Fig. 11 Synergistic catalysis in the CO_2RR. Ni@NiNCM: (a) polarization curves of Ni@NiNCM (red solid) and NiNCM (black solid) in CO_2-saturated 0.5 M $KHCO_3$ solution and the dotted lines represent those in Ar-saturated 0.5 M $KHCO_3$ solution. (b) DFT-based free energy profiles for the optimized $Ni@NiN_1CM$, $Ni@NiN_2CM$, $Ni@NiN_3CM$, and $Ni@NiN_4CM$ models during the CO_2RR. (c) A proposed reaction mechanism for CO production *via* the CO_2RR. Ni yellow, N blue, O pink, C gray, H red. Reproduced from ref. 39 with permission from Wiley-VCH GmbH, copyright 2019. Fe/Cu−N−C DAC: (d) limiting potential differences for the CO_2RR and HER on different active moieties at 0 V *vs.* RHE. Reproduced from ref. 115 with permission from the Royal Society of Chemistry, copyright 2021. Ni_2/NC DACs: (e) calculated Gibbs free energy diagrams for the CO_2RR to produce CO on various catalysts. (f) CO FE in the current density range 50−200 mA cm^{-2}. (g) Proposed reaction pathways on $O–Ni_2–N_6$. Reproduced from ref. 116 with permission from the American Chemical Society, copyright 2021. DFT calculations of SAAs: (h) Gibbs free binding energy of *CHO (ΔG_{*CHO}) against that of *H (ΔG_{*H}). The equation for the linear fitting line is $\Delta G_{*CHO} = 1.61 \times \Delta G_{*H} + 0.07$, and the correlation coefficient (R^2) is 0.90. Reproduced from ref. 119 with permission from the American Chemical Society, copyright 2016. np-Cu_1Au SAA: (i) corresponding CO FEs at different applied potentials. Reproduced from ref. 65 with permission from the American Chemical Society, copyright 2016. BiPd-SAA ND: (j) illustration of the gas diffusion flow cell for the electrochemical CO_2RR on the $C−Bi_6Pd_{94}$-SAA ND catalyst. Reproduced from ref. 120 with permission from Science China Press and Springer-Verlag GmbH Germany, part of Springer Nature, copyright 2021.

5686 | *J. Mater. Chem. A*, 2022, **10**, 5673–5698

This journal is © The Royal Society of Chemistry 2022

and 1.67 eV. For Ni$_2$/NC, a CO formation faradaic efficiency of 94.3% was achieved at 150 mA cm^{-2}, which was 1.3- and 10.6-fold higher than that of Ni$_1$/NC and NC, respectively (Fig. 11f and g). These results indicated that the O–Ni$_2$–N$_6$ can greatly lower the energy barrier of *COOH formation and improve the reactivity. Additionally, Li *et al.* synthesized a supported Pd$_2$ DAC and used it for CO$_2$ electroreduction. The as-obtained Pd$_2$ DAC exhibited superior CO$_2$RR activity with 98.2% CO faradaic efficiency at −0.85 V$_{RHE}$, far exceeding that of Pd$_1$ SAC.[117] Gong *et al.* reported the coordination of Zn and Co atoms on N doped carbon (ZnCoNC), which showed a FE$_{CO}$ of 93.2% at −0.5 V$_{RHE}$ during a 30 hours test. These studies show the great potential of DACs in CO$_2$ electroreduction application.[118]

Besides, another important expansion of the SAC series is single-atomic alloys (SAAs). In 2016, Martin *et al.* showed that SAAs are promising electrocatalysts for CO$_2$ reduction to C$_1$ hydrocarbons in aqueous solution by density functional theory calculations combined with the Poisson–Boltzmann implicit solvation model.[119] They studied 28 SAAs, and found that about half of them selectively favor the CO$_2$RR over the competing HER (Fig. 11h). The SAAs contain isolated single-atom surface sites of M (M = Cu, Ni, Pd, Pt, Co, Rh, and Ir), as surface substitutions in Au or Ag. Initial reduction of CO$_2$ to CO occurs on the Au or Ag host, and then CO binds preferentially to M, forming an internal tandem catalysis. Recently, Tan *et al.* reported a hierarchically porous Cu$_1$Au SAAs as a highly efficient catalyst for CO$_2$ electroreduction.[65] Benefiting from the hierarchically porous architectures with abundant vacancy defects, the as-prepared nanoporous Cu$_1$Au SAAs catalyst shows remarkable CO$_2$RR activity with nearly 100% CO Faraday efficiency in a wide potential range (−0.4 to −0.9 V *vs.* RHE) (Fig. 11i). This was mainly ascribed to the Cu–Au interface sites, which could facilitate the activated adsorption of CO$_2$ molecule and stabilize the *COOH intermediate. Li *et al.* reported Bi–Pd SAA nanodendrites with Bi atomically dispersed in Pd matrices for the efficient CO$_2$RR to produce CO.[120] In gas diffusion flow cells (Fig. 11j), the faradaic efficiencies of CO on the BiPd-SAA ND catalyst reach 91.8% with overpotentials of only 200 mV. The significantly enhanced activity and selectivity for CO formation on the BiPd-SAA catalyst can be attributed to the reduced surface H coverage stemming from the weaker H affinity compared to pure Pd, which inhibits H$_2$ and formate formation and decreases the reaction barrier for *COOH generation.

4.2 Synergistic single-atomic catalysis in the ORR

The oxygen reduction reaction (ORR) occurring at the cathode of fuel cells is one of the most vital reactions for energy conversion, and it is considered as the rate-limiting step in determining the overall performance of fuel cell devices due to its sluggish kinetics. The ORR proceeds through either a 4-electron pathway (O$_2$ + 4H$^+$ + 4e → 2H$_2$O) or a 2-electron pathway (O$_2$ + 2H$^+$ + 2e → H$_2$O$_2$). For metal–air batteries or fuel cell batteries, currently, an efficient catalyst could reduce oxygen directly into water through a 4e$^-$ pathway with fast kinetics. While Pt-based materials are well known as the most

active candidates toward the ORR, their intrinsic high costs limit their large-scale application.[121,122] In recent years, various transition metals, especially single-atomic catalysts (SACs), embedded in carbon-based materials have emerged as promising alternatives, which offer the advantages of fully utilized atomic sites with tunable electronic configuration and atomic coordination that facilitate the charge transfer between reactants and intermediates, thus enhancing the ORR performance.[123] It is worth noting that the metal–support interaction is most prominent for the SAC catalyst and the ORR activity could be effectively adjusted by modulating the metal–support interaction. Inspired by this, some synergistic components, such as local coordination atoms, nanoparticles, clusters, or other metal single-atoms, have been proposed to engineer the local environment of SACs, as summarized in Table 2.

Remarkably, it is reported that the introduction of some metal-based nanoparticles and/or nanoclusters makes it possible to accelerate the ORR reactivity of SACs, and it is urgent to deeply explore the synergistic effects and the nature of the catalytic processes. For example, Zhu *et al.* reported a graphene-encapsulated Fe$_3$C particle (Fe$_3$C@C) boosting Fe SAC (Fe$_3$C@C–Fe SACs) catalyst. Owing to the strong synergistic effects between Fe SACs and Fe$_3$C@C nanocrystals, Fe$_3$C@C–Fe SACs shows good ORR performance in a neutral electrolyte with the onset potential of 0.99 V and negligible activity loss after 30k cycles of durability test (Fig. 12a).[28] Moreover, Fe$_3$C@C–Fe SACs exhibits an exceptional peak power density of 74.8 mW cm^{-2} at 152.8 mA cm^{-2}, outperforming the batteries with Pt/C (40.3 mW cm^{-2} at 89.5 mA cm^{-2}) (Fig. 12b). They judged that the introduction of Fe$_3$C@C nanocrystals contributes to the adsorption of O$_2$ molecules and desorption of *OH on Fe SACs, leading to fast ORR reaction kinetics. Wu *et al.* also found a synergistic interaction between Pt NPs and surrounding FeN$_4$ sites by weakening the O$_2$ adsorption on Pt sites and reducing the activation energy to break O–O bonds, thereby enhancing the intrinsic activity of Pt.[37] Lu *et al.* reported a highly efficient and durable ORR catalyst, which consists of atomically dispersed Co single atoms (Co-SACs) in the form of Co–N$_4$ moieties and small Co nanoparticles (Co-SNPs) co-anchored on N-doped porous carbon (Co–SAs/SNPs@NC).[124] Due to the synergistic effect of Co-SACs and Co-SNPs, the resultant Co–SAs/SNPs@NC catalyst shows excellent ORR activity and stability in alkaline media, outperforming the Co–SAs-based catalyst (Co–SAs@NC) and Pt/C catalyst. Besides the synergistic effects of SACs and NPs, the contributions of SACs and clusters are also vital. For example, Fe single atoms and clusters co-embedded in N-doped carbon (Fe/NC) that deliver synergistic enhancement in pH-universal ORR catalysis were reported by Lawrence *et al.*[48] As shown in Fig. 12c, Fe/NC-3 achieves an outstanding ORR performance with a half-wave potential ($E_{1/2}$) of 0.90 V, which is superior to Pt/C (0.89 V). DFT calculations indicate that the excellent ORR performance originated from the deepened d-band center and weakened binding strength for intermediates (Fig. 12d). For the FeN$_4$/C model, 0.57 eV is required for the potential determining step (HO* + H + e$^-$ → H$_2$O + *), while the value is decreased to 0.5 eV for FeN$_4$/Fe$_4$/C, which leads to faster ORR kinetics (Fig. 12e).

This journal is © The Royal Society of Chemistry 2022

J. Mater. Chem. A, 2022, **10**, 5673–5698 | **5687**

Table 2 A summary of synergistic single-atomic catalysis in the ORR

Synergistic effect	Catalysts	Performance or parameters	Ref.
SAC-NPs	Pt_3Co/FeN_4–C	Mass activity (0.72 A mg_{Pt}^{-1}), power density (824 mW cm^{-2} at 0.67 V), and stability (23 mV loss at 1.0 A cm^{-2})	*Energy Environ. Sci.*, 2021, **14**, 4948 (ref. 37)
SAC-NPs	Co-NCS-2	Superior ORR performance with a half-wave potential ($J_{1/2}$) of 0.90 V, outperforming the commercial Pt/C	*Nano Energy*, 2021, **87**, 106153 (ref. 40)
SAC-NPs	Fe–N-HMCTs	Excellent ORR activity (onset potential, 0.992 V; half-wave potential, 0.872 V), favorable long-term stability	*Adv. Funct. Mater.*, 2021, **31**, 2009197 (ref. 42)
SAC-NPs	Fe_3C@C–Fe SAS	In neutral electrolyte with the onset potential of 0.99 V and negligible activity loss after 30k cycles	*Nano Energy*, 2021, **84**, 105840 (ref. 149)
SAC-NPs	CoSAs/SNPs@NC	Maximum power density of 223.5 mW cm^{-2}, high specific capacity of 742 W h kg^{-1} at 50 mA cm^{-2}	*Adv. Funct. Mater.*, 2021, 2104735 (ref. 124)
SACCs	Fe_{AC}@Fe_{SA}–N–C	The half-wave potential is 0.912 V *vs.* RHE, exceeding that of commercial Pt/C (0.897 V) and Fe_{SA}–N–C (0.844 V)	*ACS Nano*, 2019, **13**, 11853 (ref. 47)
SACCs	Fe/NC	The high E_{onset} of 0.97 V in base and 0.80 V in acid	*Small Methods*, 2021, 2001165 (ref. 48)
SACCs	FeCo SAs@Co/N-GC	Show superb catalytic activity with a half-wave voltage ($E_{1/2}$) of 0.88 V and a limited current density of 6.70 mA cm^{-2}	*ACS Nano*, 2021, **15**, 14683 (ref. 46)
DACs	Fe–N_4/Pt–N_4@NC	Exhibit a half-wave potential of 0.93 V and negligible activity degradation ($\Delta E_{1/2} = 8$ mV) after 10 000 cycles	*Angew. Chem., Int. Ed.*, 2021, **60**, 19262 (ref. 57)
DACs	Zn/CoN–C	ORR performance under both alkaline and acidic conditions with a half-wave potential of 0.861 and 0.796 V	*Angew. Chem., Int. Ed.*, 2019, **58**, 2622 (ref. 55)
DACs	Co_1-PNC/Ni_1-PNC	Exhibit the most positive ORR onset potential and halfwave potential ($E_{onset} = 1.00$ V, $E_{1/2} = 0.88$ V)	*Nano Res.*, 2021, **14**, 3482 (ref. 150)
DACs	Fe/Ni–N_x/OC	ORR activity with a half-wave potential ($E_{1/2}$) of 0.938 V	*Adv. Mater.*, 2020, **32**, 2004670 (ref. 126)
DACs	(Fe,Co)/N–C	Onset potential (E_{onset}, 1.06 *vs.* 1.03 V) and half-wave potential ($E_{1/2}$, 0.863 *vs.* 0.858 V)	*J. Am. Chem. Soc.*, 2017, **139**, 17281 (ref. 91)
DACs	Co–N–C-*x*	Show unprecedented catalytic activity in acidic electrolytes with a half-wave potential of 0.79 V	*Nano Energy*, 2018, **46**, 396 (ref. 151)
DACs	Cu/Zn-NC	E_{onset} of 0.98 V and an $E_{1/2}$ of 0.83 V, excellent stability (no degradation after 10 000 cycles)	*Angew. Chem., Int. Ed.*, 2021, **60**, 14005 (ref. 58)
DACs	Pt_1–Fe/Fe_2O_3	Exhibit onset and half-wave potentials of 1.15 V and 1.05 V, mass activity of 14.9 A mg_{Pt}^{-1} (at 0.95 V)	*Nat. Energy*, 2021, **6**, 614 (ref. 125)
DACs	CoFe@C	The half-wave potential approached that of Pt/C with a gap of only 32 mV	*Angew. Chem., Int. Ed.*, 2019, **58**, 1975 (ref. 152)
SAAs	Pt–Pd SAA	A mass activity of 0.91 A mg_{Pt}^{-1} at 0.9 V, which is around 4 times higher than that of the Pt/C catalyst (0.24 A mg_{Pt}^{-1})	*ACS Catal.*, 2019, **9**, 9350 (ref. 127)
SAAs	$Au_{1-x}Pd_x$/C	Increasing the Pd concentration to 8% leads to an increase of the electrocatalytic H_2O_2 production selectivity up to $\sim$95%	*J. Am. Chem. Soc.*, 2011, **133**, 19432 (ref. 153)

5688 | *J. Mater. Chem. A*, 2022, **10**, 5673–5698
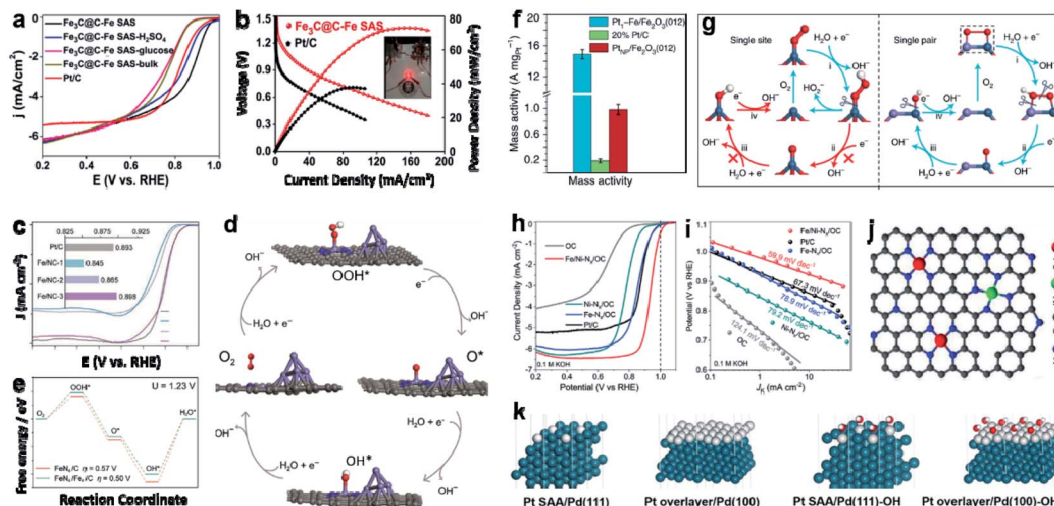
This journal is © The Royal Society of Chemistry 2022

Fig. 12 Synergistic catalysis in the ORR. Fe$_3$C@C−Fe SAS: (a) polarization curves, LSV curves and comparison of E_{onset} of various catalysts. (b) The power density curves of neutral ZABs of Fe$_3$C@C−Fe SAS and commercial Pt/C. Reproduced from ref. 28 with permission from Elsevier Ltd, copyright 2021. Fe/NC: (c) ORR polarization curves in O$_2$-saturated 1 M KOH at 1600 rpm. Inset is the half-wave potentials obtained from the polarization curves. (d) Proposed ORR mechanism in alkaline solution for the FeN$_4$/Fe$_4$/C structure. White, red, gray, blue, and purple balls represent H, O, C, N, and Fe atoms, respectively. (e) The corresponding free energy diagrams for the ORR at $U = 1.23$ V and pH = 0. Reproduced from ref. 48 with permission from Wiley-VCH GmbH, copyright 2021. Pt$_1$−Fe/Fe$_2$O$_3$: (f) comparison of mass activity at 0.95 V *versus* RHE. (g) The proposed ORR mechanism on single-site platinum and Pt−Fe pairs (violet, iron; red, oxygen; dark blue, platinum; white, hydrogen). Reproduced from ref. 125 with permission from the author(s), under exclusive license to Springer Nature Limited, copyright 2021. Fe/Ni−N$_x$/OC: (h) the ORR polarization curves of Fe/Ni−N$_x$/OC, Fe−N$_x$/OC, Ni−N$_x$/OC, OC, and Pt/C in O$_2$-saturated 0.1 M KOH at a rotating rate of 1600 rpm, and (i) the corresponding Tafel plots. (j) Proposed structural model of Fe/Ni−N$_x$/OC. Reproduced from ref. 126 with permission from Wiley-VCH GmbH, copyright 2020. Pt/Pd SAA: (k) most stable adsorption configurations of OH on Pt-SAA/Pd(111) and PtOL/Pd(100). Reproduced from ref. 127 with permission from the American Chemical Society, copyright 2020.

In addition, the introduction of a second metal atom can enhance the activity of SACs due to the presence of more catalytic sites, which bodes well for the expansion of dual-atom site catalysts (DACs). For example, Zou *et al.* loaded platinum onto α-Fe$_2$O$_3$ to construct a highly active ORR catalyst with dispersed Pt−Fe pair sites, which show a high mass activity of 14.9 A mg$_{\text{Pt}}^{-1}$ at 0.95 V (Fig. 12f).[125] A detailed ORR reaction path on a single-site Pt−Fe pair is illustrated in Fig. 12g, suggesting that the ORR kinetics is mostly attributed to easy O$_2$ activation on a single-site Pt−Fe pair and OH* desorption on single-site platinum. Zhao *et al.* also reported a hetero-single-atomic ORR catalyst with atomically dispersed Fe and Ni co-anchored to N-doped graphitic carbon (denoted as Fe/Ni−N$_x$/OC).[126] For comparison, the ORR performances of Fe/Ni−N$_x$/OC, OC, Ni−N$_x$/OC, Fe−N$_x$/OC, and Pt/C were evaluated together. Among them, as shown in Fig. 12h, Fe/Ni−N$_x$/OC exhibits the best ORR activity with a half-wave potential ($E_{1/2}$) of 0.938 V, which is 267, 90, 84, and 66 mV higher than that of OC ($E_{1/2} = 0.671$ V), Ni−N$_x$/OC ($E_{1/2} = 0.848$ V), Fe−N$_x$/OC ($E_{1/2} = 0.854$ V), and the benchmark Pt/C ($E_{1/2} = 0.872$ V), respectively. The excellent ORR activity of Fe/Ni−N$_x$/OC can be further evidenced by its smallest Tafel plot slope (59.9 mV dec^{-1}) among all the investigated samples (Fig. 12i and j). In addition to the carbon support, the metal single atoms could also be located on the surface of a different metal, which is named single-atom alloys (SAAs). As one typical kind of single-atom catalysts, Pt-based SAAs have gained great interest due to their unique advantages in the ORR. For instance, Botton and Sun *et al.* successfully prepared octahedral

Pt/Pd SAA catalysts,[127] with the formation of an alloy structure. The ORR activities of the Pt atom could be improved due to the synergistic effect of Pt and Pd. Furthermore, they used DFT calculations to probe the enhanced mechanism of the Pt atoms on Pd surfaces with different structures during the ORR processes, revealing that the Pt/Pd SAA structure could weaken the interaction between OH* and surface Pt atoms, and the desorption of OH* is the rate-determining step (Fig. 12k). All in all, these studies open up a new avenue to develop new types of metal-based catalysts for the ORR and bring a new understanding about the synergistic mechanism of single-atomic catalysts.

4.3 Synergistic single-atomic catalysis in the HER

Water splitting provides an efficient and sustainable route for clean hydrogen energy and the production of H$_2$. Particularly, the HER is a two electron transfer reaction taking place on the electrode surface through two steps ($2H^+ + 2e^- \rightarrow H_2$), consisting of the adsorption of hydrogen (Volmer reaction) and the desorption of H* (Heyrovsky or Tafel reactions).[128,129] The first step (Volmer or discharging reaction) of the HER is discharging protons (H$^+$) to form an absorbed hydrogen intermediate (H$_{\text{ads}}$) by coupling with an electron on the active surface of an electrode, and in the second step, H$_2$ gas forms *via* two different mechanisms (Heyrovsky or Tafel reactions), depending on the H$_{\text{ads}}$ coverage on the electrode surface. According to the Nørskov principle, a good HER catalyst should bond to

This journal is © The Royal Society of Chemistry 2022

J. Mater. Chem. A, 2022, **10**, 5673–5698 | **5689**

adsorbed H* with sufficient strength to facilitate the proton–electron-transfer process. While Pt-based catalysts meet the design principle and exhibit the most remarkable HER activity, their scarcity and high cost significantly limit their commercial applications.[130] Thus, it remains a huge challenge to develop highly efficient and low-priced hydrogen evolution electrocatalysts. Reducing the size of the metal NPs to clusters or even single atoms could significantly decrease the noble metal usage and increase their catalytic activity; nevertheless, the isolated single atoms are unstable and usually anchored on specific supports by chemical bonding with surrounding atoms.[131,132] Therefore, the catalytic activities of SACs highly depend on the local coordination environment of metal centers (the geometric and electronic interactions between metal atoms and their supports). To further increase the metal active center, the coexistence of transition metal atoms and nanoparticles (NPs) or clusters was developed and has been proved to further optimize the catalytic ability, as summarized in Table 3. For example, Wang et al. proposed an efficient strategy to construct porous N-doped carbon fiber supported Ni SACs and NP hybrid with accessible active sites (Ni SA/NP-NCF-800).[133] The unique

configuration endows the hybrid with outstanding hydrogen evolution performance along with the low overpotential (137.3 mV to afford 10 mA cm^{-2}) and robust long-term durability in alkaline media. They further revealed that the synergistic effect of atomically dispersed Ni and nanoparticles could optimize H adsorption free energy and enhance water adsorption/dissociation abilities. In addition, Su et al. designed a hybrid HER catalyst (Ru/Co@OG), comprising both Ru nanoparticles and dispersed metal atoms, which exhibited an ultralow Tafel slope of 22.8 mV dec^{-1} and low overpotential of 13 mV at a current density of 10 mA cm^{-2}. To better understand the enhanced HER performance of Ru/Co@OG, the free adsorption energy for H* species (ΔG_{H*}) and kinetic barrier for water dissociation (E_a) are taken into account to characterize the HER activity in alkaline media.[134] As shown in Fig. 13a and b, Ru/Co@OG shows optimal adsorption strength towards H species with ΔG_{H*} of -0.05 to 0.05 eV, and the activities of Ru nanoparticles and single metal atoms on substrates show a clear linear relationship with the d band center, as evident in Fig. 13b. According to the d band theory, a lower d band center corresponds to more occupancy of the antibonding state between the catalyst and H* adsorbate,

Table 3 A summary of synergistic single-atomic catalysis in the HER

Synergistic effect	Catalysts	Performance or parameters	Ref.
SAC-NPs	Ni SA/NP-NCF	A low overpotential of 137.3 mV to afford 10 mA cm^{-2}, a high turnover frequency of 0.077 s^{-1} at 200 mV	*Carbon.*, 2021, **185**, 96 (ref. 113)
SAC-NPs	Ru/Co@OG	An overpotential of 13 mV at a current density of 10 mA cm^{-2} and ultralow Tafel slopes of 22.8 mV dec^{-1}	*Angew. Chem., Int. Ed.*, 2021, **60**, 16044 (ref. 134)
SACCs	Ru–C$_5$ SACs@Ru–O$_4$ clusters	Largely boosts alkaline HER with only an overpotential of 18 mV at 10 mA cm^{-2}	*Small*, 2021, 2101163 (ref. 34)
SACCs	Pt$_{0.2}$–CeO$_2$	The mass activity of Pt$_{0.2}$–CeO$_2$ for the HER is around 50 times that of Pt/C	*Electrochim. Acta*, 2019, **297**, 155 (ref. 154)
SACCs	ALDPt/NGNs	The mass activity of the HER for the ALDPt/NGNs catalysts at the overpotential of 0.05 V was 10.1 A mg^{-1}	*Nat. Commun.*, 2016, **7**, 13638 (ref. 49)
DACs	Ru/Ni–MoS$_2$	Exhibited a super-low overpotential of 32 mV at 10 mA cm^{-2} with the corresponding Tafel slope of 41 mV dec^{-1}	*Appl. Catal., B*, 2021, **298**, 120557 (ref. 84)
DACs	W$_1$Mo$_1$–NG	Produce a cathodic geometric current density (j) of 10 mA cm^{-2} at an overpotential of 24 mV	*Sci. Adv.*, 2020, **6**, eaba6586 (ref. 51)
SAAs	np-Cu$_{53}$Ru$_{47}$	Achieving 10 mA cm^{-2} at low overpotentials of ~15 and ~41 mV in both alkaline and neutral electrolytes	*ACS Energy Lett.*, 2020, **5**, 192 (ref. 66)
SAAs	Pt–Pd SAA	The mass HER activity for the octahedral Pt/Pd SAA catalysts at the overpotential of 0.05 V is 23.5 A mg^{-1}	*ACS Catal.*, 2019, **9**, 9350 (ref. 127)
SAAs	RuAu SAAs	Exhibit a high stability and a low overpotential of 24 mV @ 10 mA cm^{-2}	*Adv. Energy Mater.*, 2019, 1803913 (ref. 135)

5690 | *J. Mater. Chem. A*, 2022, **10**, 5673–5698

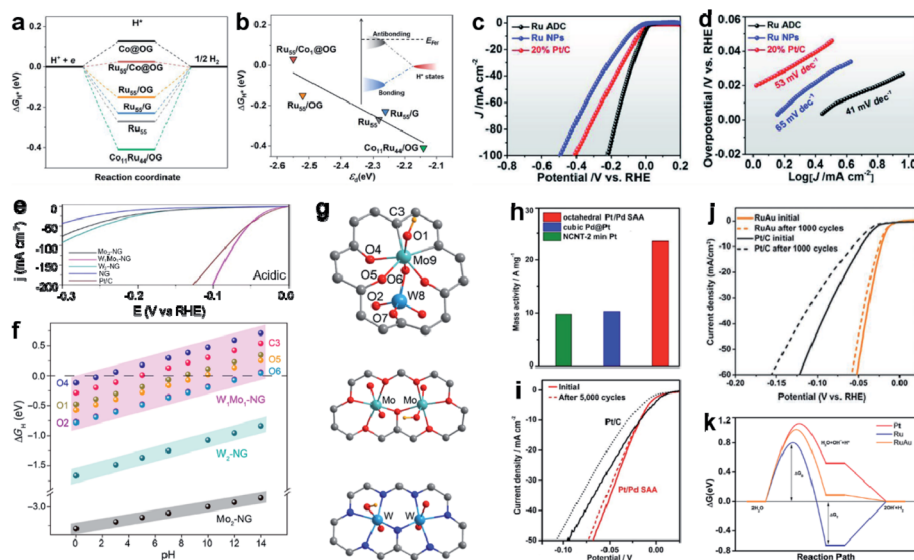This journal is © The Royal Society of Chemistry 2022

Fig. 13 Synergistic catalysis in the HER. Ru/Co@OG: (a) free energy diagrams for hydrogen evolution at zero potential and pH = 0 on various catalysts by DFT calculation. (b) ΔG_{H*} as a function of the d band center of transition metal atoms (the inset is a schematic illustration of bond formation between the supported metal nanoparticle and adsorbed H* species). Reproduced from ref. 134 with permission from the authors and Wiley-VCH GmbH, copyright 2021. Ru ADC: (c) LSV curves for alkaline HER. (d) Tafel plots of samples. Reproduced from ref. 34 with permission from Wiley-VCH GmbH, copyright 2021. W_1Mo_1–NG: (e) the polarization curves and corresponding Tafel plots of Mo_2–NG, W_1Mo_1–NG, W_2–NG, NG, and Pt/C in 0.5 M H_2SO_4. (f) ΔG_H diagrams of W_1Mo_1–NG, Mo_2–NG, and W_2–NG. (g) Optimized geometries and possible sites for H adsorption on W_1Mo_1–NG, Mo_2–NG, and W_2–NG systems. Atom colors: cyan, Mo; royal blue, W; dark gray, C; blue, N; red, O; orange, H. Reproduced from ref. 51 with permission from the authors and exclusive licensee American Association for the Advancement of Science, copyright 2021. Pt–Pd SAA: (h) normalized mass activity at 0.05 V. (i) Durability measurement of the octahedral Pt–Pd SAA catalysts and commercial Pt/C catalysts. Reproduced from ref. 127 with permission from the American Chemical Society, copyright 2019. RuAu SAA: (j) durability test. (k) Gibbs free energy profile of the HER on Pt (111), Ru (001), and RuAu (001) surfaces. ΔG_T represents the energy barrier for the Heyrovsky reaction. ΔG_B represents the activation energy of water dissociation. Reproduced from ref. 135 with permission from Wiley-VCH GmbH, copyright 2019.

which results in weaker but more optimal H* binding strength for hydrogen evolution.

Coupling multi-active sites into one catalyst for the hydrogen evolution reaction is a direct method to compensate for the drawback of single-site catalysts. In addition to the coexistence of nanoparticles with single-atomic sites, monodisperse nanoclusters could enhance the synergistic effect. For instance, Cheng *et al.* constructed a Ru atomically dispersed catalyst (Ru ADC) with Ru–C_5 single atoms and Ru oxide nanoclusters (≈ 1.5 nm).[34] It was found that the obtained Ru ADC largely boosts alkaline hydrogen evolution by concerted catalysis between single atoms and sub-nanoclusters. Fig. 13c shows that Ru ADC only needs an overpotential of 18 mV to obtain a current density of 10 mA cm^{-2}, while Ru NPs and 20% Pt/C require overpotentials of 98 and 46 mV, respectively. In addition, the Tafel slope of Ru ADC is 41 mV dec^{-1}, which is smaller than that of Ru NPs (53 mV dec^{-1}) and 20% Pt/C (65 mV dec^{-1}), as shown in Fig. 13d. It can be seen that Ru ADC with highly active monodispersed clusters and single sites can display excellent HER activity. The synergetic catalysis process is described as follows: (i) Ru–C_5 single atoms provide spaces for efficient capture of water molecule. (ii) The coupling of Ru–O_4 nanoclusters and Ru–C_5 single atom is responsible for the destabilization of bonds in the water molecule, favoring its dissociation into H and OH. This study opens up a simple strategy to tune dual-atom sites.

Compared to single-atom components, multiatom catalysts with tunable electronic states could further improve the intrinsic activity and stability. In a multiatom catalytic system, the strong chemical interactions between neighboring atoms can efficiently stabilize the individual species and prevent agglomeration. Within this context, dispersing metal atoms on a support into a cluster or dinuclear type could improve the catalytic activity by tuning the coordination number (CN), ligand atom, and structural distortion. Recently, Fan *et al.* developed a dual-atom catalyst (DAC) consisting of an O-coordinated W–Mo heterodimer embedded in N-doped graphene (W_1Mo_1–NG), which enables Pt-like activity and ultrahigh stability for the HER in a pH-universal electrolyte.[51] As illustrated in Fig. 13e, W_1Mo_1–NG exhibits excellent HER activity, giving a near-zero onset potential (U_{onset}) in acidic electrolytes, and produces cathodic geometric current density (j) of 10 mA cm^{-2} at an overpotential of 24 mV. By comparing the ΔG_H of homonuclear Mo_2–NG, W_2–NG and W_1Mo_1–NG (Fig. 13f and g), we can see that the heteronuclear W_1Mo_1–NG with diverse binding sites is more active than the homonuclear catalysts. In addition to the carbon support, metal single atoms can also be located on the surface of a different metal, which is named single-atom alloys (SAAs). Botton *et al.* successfully prepared octahedral Pt/Pd SAA catalysts,[127] which exhibited greatly improved HER activity compared to commercial Pt/C. The mass HER activity for the octahedral Pt/Pd SAA

catalysts at the overpotential of 0.05 V is 23.5 A mg^{-1}, which is 54.6 times greater than that of the Pt/C catalysts (0.43 A mg^{-1}) (Fig. 13h). Moreover, due to the strong interaction between Pt atoms with Pd surface, the Pt/Pd SAA catalysts exhibited better stability than the Pt/C catalysts, as exhibited in Fig. 13i. Du *et al.* also reported a novel RuAu SAA, which exhibits high stability and low overpotential in alkaline media (Fig. 13j).[135] The superior HER activity and stability are also attributed to the relatively high total unoccupied density and the synergistic effect of stable metallic Au on Ru particles (Fig. 13k). In future, a clear insight into the synergistic catalytic process between metal components and isolated metal sites in one catalyst is necessary.

4.4 Synergistic single-atomic catalysis in the OER

The water-splitting reaction consists of two key half reactions: the cathodic HER: $2H^+ + 2e^- \rightarrow H_2$ and anodic OER: $2H_2O \rightarrow O_2 + 4H^+ + 4e^-$ in acidic electrolytes or $4OH^- \rightarrow 2H_2O + O_2 + 4e^-$ under neutral or alkaline conditions. Currently, the critical bottleneck of water splitting is the oxygen evolution reaction (OER) due to the high thermodynamic potential and sluggish kinetics compared to the HER.[136] Besides, the OER also plays an important role in rechargeable batteries, such as zinc–air and lithium–air batteries. However, the intense degradation of catalysts in low pH and the strong oxidative environment seriously impede its practical application. Various efforts have been

devoted to develop heterogeneous OER catalysts with excellent reactivity and stability. However, the heterogeneous nature of these catalysts makes it hard to explore the nature of their active sites.[137] Single-atomic catalysis has emerged as an efficient way to combine the single-site nature of homogeneous catalysis with the high selectivity of heterogeneous catalysis. Compared to single-atomic catalysts, dual-atomic catalysts would be more active for the oxygen evolution reaction, as summarized in Table 4. For example, Hu *et al.* reported a Co–Fe double-atom catalyst (Co–Fe–N–C), which exhibits turnover frequencies (TOFs) comparable to those of state-of-the-art OER catalysts.[138] Such a dual-atomic catalyst bridges the transitionally separated molecular and solid-sate catalysts, and provides an attractive platform for fundamental studies of metal sites in the OER. Lee *et al.* constructed a FeCo dual-site catalyst (FeCo$_{SAs}$@Co/N-GC), which shows exceptional OER activity, reversible redox kinetics, and durability in universal pH environments.[46] As shown in Fig. 14a, FeCo$_{SAs}$@Co/N-GC demonstrated the lowest overpotential ($E_{j=10}$) of 0.29 V, outperforming that of RuO$_2$ ($E_{j=10}$ = 330 mV). Moreover, FeCo$_{SAs}$@Co/N-GC displayed 10 000 CV cycle stability with negligible loss of overpotential (Fig. 14b). Additionally, Chen *et al.* demonstrated a diatomic NiFe catalyst supported by nitrogen-doped graphene (NiFe-DACs) with extraordinary and stable electrocatalytic performance towards the OER (10 mA cm^{-2} at an overpotential of 310 mV) (Fig. 14c).[56]

Table 4 A summary of synergistic single-atomic catalysis in the OER and N$_2$RR

| Synergistic effect	Catalyst	Performance or parameters	Ref.
OER			
SACCs	FeCo$_{SAs}$@Co/N-GC	Demonstrated the overpotential ($E_{j=10}$) of 0.29 V plus a Tafel value of 56.6 mV dec^{-1}	*ACS Nano*, 2021, **15**, 14683 (ref. 46)
DACs	Co–Fe–N–C	The overpotential at 10 mA cm^{-2} was 309 mV	*J. Am. Chem. Soc.*, 2019, **141**, 14190 (ref. 138)
DACs	Fe$_2$-GNCL	The Tafel slope of Fe$_2$-GNCL (66 mV dec^{-1}) is much smaller than that of Fe$_3$-NPs/GNCL (137 mV dec^{-1})	*Angew. Chem., Int. Ed.*, 2020, **59**, 16013 (ref. 59)
DACs	NiFe-DACs	Achieve a current density of 10 mA cm^{-2} at a low potential of +1.54 V *vs.* RHE	*Nat. Commun.*, 2021, **12**, 4088 (ref. 56)
DACs	Ni$_1$/Ni$_2$- and Fe$_1$/Ni$_2$-DACs	The OER activity of Ni$_1$/Ni$_2$–Ti$_2$CO$_2$ is even better than that of landmark Pt(111) and IrO$_2$(110) catalysts	*Adv. Mater.*, 2021, 2102595 (ref. 73)
SAAs	Ru$_1$–Pt$_3$Cu	Deliver 90 mV lower overpotential to reach a current density of 10 mA cm^{-2}	*Nat. Catal.*, 2019, **2**, 304 (ref. 139)
N$_2$RR			
SAC-NPs	MoSAs–Mo$_2$C	Yields an ammonia formation rate of 16.1 μg h^{-1} cm$_{cat}^{-2}$ at −0.25 V *vs.* RHE	*Adv. Mater.*, 2020, **32**, 2002177 (ref. 41)
SACCs	Co$_1$Ru TCs	Show the highest NH$_3$ synthesis rate (up to 21.9 mmol NH$_3$ g^{-1} h^{-1} at 360 °C and 3 MPa) among the Ru or Co-based catalysts	*ACS Catal.*, 2021, **11**, 4430 (ref. 43)
DACs	M$_1$M$_2$N$_6$–NG	Mo–Ru, Mo–Co, Mo–W, Mo–Fe and Fe–Ru dimers exhibited onset potentials of only 0.17, 0.27, 0.28, 0.36 and 0.39 V	*J. Catal.*, 2020, **388**, 77 (ref. 155)
DACs	PdCu/NC	Achieve a high FE of 24.8 ± 0.8% and a desirable NH$_3$ yield rate of 69.2 ± 2.5 mg h^{-1} mg$_{cat}^{-1}$	*Angew. Chem., Int. Ed.*, 2021, **60**, 345 (ref. 107)
DACs	M$_2$–Pc BACs	Ti$_2$–Pc, V$_2$–Pc, TiV–Pc, VCr–Pc, and VTa–Pc, can suppress the competitive HER with a favorable limiting potential of −0.75, −0.39, −0.74, −0.85, and −0.47 V	*J. Am. Chem. Soc.*, 2020, **142**, 5709 (ref. 106)
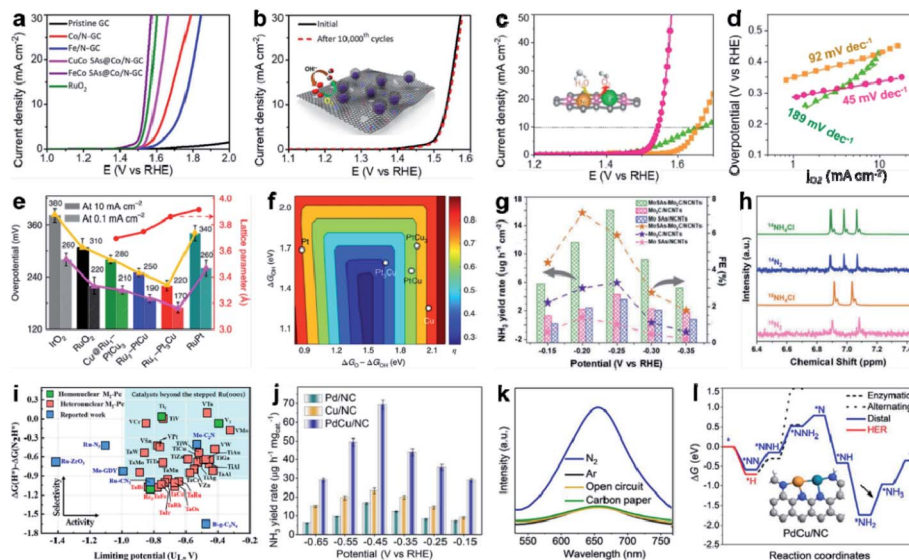
Fig. 14 Synergistic catalysis in the OER. FeCo SAs@Co/N-GC: (a) LSV profiles for the OER. (b) OER LSV profiles of FeCo SAs@Co/N-GC initially and after 10 000 continuous cycles. Reproduced from ref. 46 with permission from the American Chemical Society, copyright 2021. NiFe-DACs: (c) LSV curves, and (d) Tafel plots for the OER in O_2-saturated 1.0 M KOH at a rotation speed of 1600 rpm and a scan rate of 1 mV s^{-1}. Reproduced from ref. 56 with permission from the author(s), copyright 2021. $Ru_1–Pt_3Cu$: (e) overpotential to reach 0.1 mA cm^{-2} and 10 mA cm^{-2} for the catalysts (left axis) and lattice parameter dependence on the composition of Pt/Cu (right axis, red line). Error bars show the s.d. evaluated from five independent measurements. (f) Calculated volcano plot of OER overpotential η with ΔG_{OH} and $\Delta G_O - \Delta G_{OH}$ as descriptors. Reproduced from ref. 139 with permission from the author(s), under exclusive license to Springer Nature Limited, copyright 2019. Synergistic catalysis in the N_2RR. $Mo_{SAs}–Mo_2C/NCNTs$: (g) the NH_3 yield rate and FE of various samples. (h) ^1H NMR spectra of the electrode after 12 h of electrochemical reduction using $^{15}N_2$ as the feed gas. Reproduced from ref. 41 with permission from Wiley-VCH GmbH, copyright 2020. $M_2–Pc$ BACs: (i) limiting potential (U_L) versus $\Delta G(H^*) - \Delta G(N_2H^*)$ on 31 $M_2–Pc$ and 6 reported catalysts. Reproduced from ref. 106 with permission from the American Chemical Society, copyright 2020. PdCu/NC: (j) NH_3 yield rates of PdCu/NC, Pd/NC, and Cu/NC at each given potential in N_2-saturated 0.05 M H_2SO_4. (k) UV-vis absorption spectra of electrolytes stained with indophenol blue indicator after the N_2RR on PdCu/NC, carbon paper, Ar control experiment, and under open circuit conditions at −0.45 V vs. RHE. (l) Calculated free-energy diagrams of the N_2RR and HER on PdCu/NC systems. Reproduced from ref. 107 with permission from Wiley-VCH GmbH, copyright 2021.

Moreover, NiFe-DAC has the lowest Tafel slope (45 mV dec^{-1}) as compared with Ni-SAC (92 mV dec^{-1}) and Fe-SAC (189 mV dec^{-1}) (Fig. 13d), indicating the fastest reaction kinetics. Such exceptional performance is attributed to the orbital coupling between the catalytic Fe center and the adjacent Ni atom, leading to a higher oxidation state of Fe. Besides carbon-based supports, Li et al. constructed a series of alloy-supported Ru_1 based on different PtCu alloys, and found a volcano relationship between the OER activity and the lattice constant of the PtCu alloys.[139] As illustrated in Fig. 14e, the OER overpotential of $Ru_1–Pt_3Cu$ at the inverse-volcano peak outperformed the state-of-the-art RuO_2 (310 mV) and IrO_2 (380 mV) catalysts in acidic electrolytes. Moreover, the calculated overpotential η can be represented by a 2D volcano-type surface with respect to the free energy of the O and OH intermediates (Fig. 14f). They further revealed that the compressive strain of the Pt skin shell adjusts the electronic structure of the Ru_1, leading to an optimal binding of oxygen species. These examples demonstrate the importance of metal synergistic components for improving single-atom catalytic activity.

4.5 Synergistic single-atomic catalysis in the N_2RR

The electrochemical nitrogen reduction reaction (N_2RR) emerges as a promising route for the synthesis of ammonia

(NH_3) compared to the energy-consuming Haber–Bosch process (reaction conditions: high temperature of 300–500 °C and pressure of 200–300 atm).[140,141] The N_2RR involves a six-electron and a six-proton transfer process ($N_2 + 6H^+ + 6e^- \rightarrow 2NH_3$ or $N_2 + 3H_2O \rightarrow 2NH_3 + 3/2O_2$), which is a rather complex reaction inclusive of the adsorption/activation of N_2 and desorption of NH_3. Currently, the major bottleneck of NH_3 synthesis under electrochemical conditions is: (i) the relatively poor activity, originating from the sluggish adsorption of N_2 and high cleavage energy of the $N≡N$ triple bonds (941 kJ mol^{-1}), and (ii) the low selectivity due to the competing HER process.[142,143] Therefore, it is relatively difficult to construct a N_2RR catalyst with both high catalytic activity and selectivity. Besides, another restrictive factor of the N_2RR is the scaling relation in which the feasibility of N_2 dissociative adsorption on a catalyst is inversely related to that of the desorption of surface N-containing intermediates. In order to realize high Faraday efficiency (FE), tremendous efforts have been devoted to seek for catalytic materials that can overcome the scaling relations.

Recent research studies have shown that the surface d-band center of transition-metals (TMs) is closely related to the binding strength of N-containing intermediates. Among all reported TM catalysts, SACs with a narrow d-band have exhibited promising perspectives due to their maximized atom utilization

and unsaturated coordination configuration.[144] Furthermore, when nanoparticles or nanoclusters (with a broad d-band) and SACs coexist in a catalyst, it is also more likely to break the scaling relationship, as summarized in Table 4. For example, John et $al.$ reported a unique synergistic strategy in the catalyst consisting of both MoSAs and Mo_2C nanoparticles grown on a N-doped carbon nanotube support (MoSAs–Mo_2C/NCNTs),[41] while both the N_2RR activity (16.1 µg h^{-1} cm_{cat}^{-2} at −0.25 V) and selectivity (FE $\sim$ 7.1%) are greatly improved compared to those of Mo_2C/NCNTs (4.3 µg h^{-1} cm_{cat}^{-2}, 3.6%) and MoSAs/NCNTs (3.3 µg h^{-1} cm_{cat}^{-2}, 1.4%), as evidenced by the $^{14}N_2$ and $^{15}N_2$ isotope labeling nuclear magnetic resonance (NMR) spectra (Fig. 14g and h). Huang et $al.$ introduced a descriptor-based design principle to investigate the large composition space of dual-atomic catalysts (DACs) toward the N_2RR under acidic conditions. The $\Delta G(H^*) - \Delta G(N_2H^*)$ $vs.$ U_L relationship for the 31 promising N_2RR catalysts (3 homonuclear and 28 heteronuclear DACs) is shown in Fig. 14i.[106] Based on this selectivity criterion, a catalyst with a positive $\Delta G(H^*) - \Delta G(N_2H^*)$ value (>0) indicates a significant preference for hydrogenation of N_2^* and thus presents good selectivity. Consistent with the results of this DFT prediction, Xin et $al.$ designed a catalyst with diatomic Pd–Cu sites on N-doped carbon by modulation of single-atom Pd sites with Cu.[107] The introduction of Cu can not only facilitate the hydrogen dissociation at Pd sites but also enhance the electron transfer rate by strong d–d coupling with Pd toward an excellent N_2RR. As shown in Fig. 14j, NH_3 yields over the PdCu/NC catalyst increase with more negative potential until reaching −0.45 V, where the maximum value of NH_3 yield rate is calculated as 69.2 ± 2.5 µg h^{-1} mg_{cat}^{-1}, 4.2 and 3.0 times of Pd/NC and Cu/NC, respectively. These results are confirmed by UV-vis absorption spectra of electrolytes stained with indophenol blue indicator after the N_2RR (Fig. 14k). In addition, PdCu/NC shows a much lower free-energy change for the *NNH formation (ΔG_{*NNH}), leading to a substantial enhancement in N_2RR activity compared to Pd/NC and Cu/NC (Fig. 14l). Recently, Jiang et $al.$ constructed a Co–Ru alloy catalyst with atomically dispersed Co deposits onto the surface of Ru tiny subnanoclusters (Co_1Ru TCs),[132] and proved that Co_1Ru TCs instead of single Ru atoms or large Ru clusters can repel the adsorption of nitrogen-containing intermediates on the catalyst surface. These findings may further inspire the design of highly efficient single atom-based electrocatalysts toward the N_2RR.

5. Conclusions and perspectives

Owing to their unique atomic dispersion, quantum size effect, unsaturated coordination environment, and tunable electronic structure, SACs have not only been employed as efficient electrocatalysts to explore the structure–property relationship more deeply, but are also regarded as an ideal platform to bridge the gap between heterogeneous and homogeneous catalysis. However, SACs also suffer from some intrinsic drawbacks, such as low metal loading, aggregation, and isolated single active sites, which hinder their further development. As illustrated in the foregoing sections, when the size of the central metal atom

is minimized into sub-nano clusters or single atoms, the coordination states of these atomically dispersed metal species play a key role in determining the overall catalytic performance, involving activity, selectivity, and stability. Moreover, the local environment of active centers is considered to dominate the intrinsic catalytic activity, which could be intentionally regulated by rational designs and the coupling of some synergistic components. Derived from SACs, SAC-NPs, SACCs, DACs and SAAs can increase the number of active centers and improve the strong metal–support interaction (SMSI) while still maintaining their atomic dispersion. Besides, the coordination and synergistic effect between metal atoms could more accurately tune the electronic structure, and optimize the catalytic performance. As a new expansion branch of single-atom catalysts, SAC-NPs, SACCs, DACs and SAAs have tremendous potential to overcome the intrinsic drawbacks of SACs and further understand the fundamental catalytic process at the atomic level. In this review, we summarized the recent research progress of SAC-NPs, SACCs, DACs and SAAs, including the categories, synthetic strategies and characterization techniques to determine the active center. Later, the effects of coupling-microstructure and synergistic effect on the electrocatalytic performance are further probed. Finally, we systematically summarized and compared the similarities and differences between SACs and SAC-NPs/SACCs/DACs/SAAs, and emphasized the remarkable effects of adding these synergistic components.

Nevertheless, the evolution of synergistic catalysis between different components and single atoms is still in its infancy, and many challenges need to be tackled in the next stage of research. First, besides the synergistic effect of dual sites, the three- or multiple-sites are worthy of attention. For instance, during the electrochemical reaction, some metal components will be transformed into single atoms or clusters in $situ$, which may present different geometric and electronic characteristics. Second, it is still hard to obtain uniform active sites of SAC-NPs, SACCs, DACs, and SAAs at the atomic level. For example, although DACs could increase the loading amounts of active sites compared with SACs, the excessive metal loading would still cause atomic aggregation and reconstruction. In addition, the uneven defects and holes of supports during the synthetic process make it hard to precisely control the exact configuration and uniform dispersion of single-atomic alloys. Thus, aggregated nanoparticles or clusters inevitably appear on the supports coupling with single-atomic sites (SAC-NPs and SACCs). Third, to monitor the evolution and real chemical state of single-atomic coordination sites during the electrocatalytic reaction, $operando$ liquid phase-transmission electron microscopy and in $situ$ X-ray absorption spectroscopy are effective in providing real-time structural information of intermediates. Changes in the surrounding environments of multiple sites during the reaction process lead to variations of chemical bonds and surface charge distributions. Recent studies have revealed that SAAs would suffer from heavy surface oxidation and protonation in acidic or alkaline medium. Accordingly, it is essential to build the relationships between reaction stabilities and local coordination environments. Summarily, although the practical application of SAC-NPs/SACCs/DACs/SAAs still face

many challenges (including the precise synthesis, accurate active sites identify, real-time reaction observation and clear mechanism analysis), they have been at the research frontier and provide a new route to design more effective catalytic materials.

Author contributions

Both F. Y and W. X. contributed to the writing of the manuscript.

Conflicts of interest

The authors declare no competing financial interest.

Acknowledgements

References

1 Y. Y. Birdja, E. Pérez-Gallent, M. C. Figueiredo, A. J. Göttle, F. Calle-Vallejo and M. T. M. Koper, *Nat. Energy*, 2019, **4**, 732–745.

2 S. Nitopi, E. Bertheussen, S. B. Scott, X. Liu, A. K. Engstfeld, S. Horch, B. Seger, I. E. L. Stephens, K. Chan, C. Hahn, J. K. Nørskov, T. F. Jaramillo and I. Chorkendorff, *Chem. Rev.*, 2019, **119**, 7610–7672.

3 K. Jiao, J. Xuan, Q. Du, Z. Bao, B. Xie, B. Wang, Y. Zhao, L. Fan, H. Wang, Z. Hou, S. Huo, N. P. Brandon, Y. Yin and M. D. Guiver, *Nature*, 2021, **595**, 361–369.

4 Y. Li, H. H. Wang, C. Priest, S. W. Li, P. Xu and G. Wu, *Adv. Mater.*, 2021, **33**, 2000381.

5 X. C. Yan, L. Z. Zhuang, Z. H. Zhu and X. D. Yao, *Nanoscale*, 2021, **13**, 3327–3345.

6 H. Wang and J. M. Lee, *J. Mater. Chem. A*, 2020, **8**, 10604–10624.

7 Y. Chen, S. Ji, C. Chen, Q. Peng, D. Wang and Y. Li, *Joule*, 2018, **2**, 1242–1264.

8 A. Beniya and S. Higashi, *Nat. Catal.*, 2019, **2**, 590–602.

9 X.-F. Yang, A. Wang, B. Qiao, J. Li, J. Liu and T. Zhang, *Acc. Chem. Res.*, 2013, **46**, 1740–1748.

10 C. Z. Zhu, S. F. Fu, Q. R. Shi, D. Du and Y. H. Lin, *Angew. Chem., Int. Ed.*, 2017, **56**, 13944–13960.

11 S. Mitchell, E. Vorobyeva and J. Perez-Ramirez, *Angew. Chem., Int. Ed.*, 2018, **57**, 15316–15329.

12 X.-L. Lu, X. Rong, C. Zhang and T.-B. Lu, *J. Mater. Chem. A*, 2020, **8**, 10695–10708.

13 T. N. Nguyen, M. Salehi, Q. V. Le, A. Seifitokaldani and C. T. Dinh, *ACS Catal.*, 2020, **10**, 10068–10095.

14 J. Feng, H. Gao, L. Zheng, Z. Chen, S. Zeng, C. Jiang, H. Dong, L. Liu, S. Zhang and X. Zhang, *Nat. Commun.*, 2020, **11**, 4341.

15 Q. Liu, Y. Wang, Z. Hu and Z. Zhang, *RSC Adv.*, 2021, **11**, 3079–3095.

16 S. Back, J. Lim, N.-Y. Kim, Y.-H. Kim and Y. Jung, *Chem. Sci.*, 2017, **8**, 1090–1096.

17 M.-M. Millet, G. Algara-Siller, S. Wrabetz, A. Mazheika, F. Girgsdies, D. Teschner, F. Seitz, A. Tarasov, S. V. Levchenko, R. Schlögl and E. Frei, *J. Am. Chem. Soc.*, 2019, **141**, 2451–2461.

18 B. You, X. Liu, G. Hu, S. Gul, J. Yano, D.-e. Jiang and Y. Sun, *J. Am. Chem. Soc.*, 2017, **139**, 12283–12290.

19 A. Q. Wang, J. Li and T. Zhang, *Nat. Rev. Chem.*, 2018, **2**, 65–81.

20 B. Peng, H. Liu, Z. Liu, X. Duan and Y. Huang, *J. Phys. Chem. Lett.*, 2021, **12**, 2837–2847.

21 N. C. Cheng, L. Zhang, K. Doyle-Davis and X. L. Sun, *Electrochem. Energy Rev.*, 2019, **2**, 539–573.

22 J. W. Su, R. X. Ge, Y. Dong, F. Hao and L. Chen, *J. Mater. Chem. A*, 2018, **6**, 14025–14042.

23 F. Franco, C. Rettenmaier, H. S. Jeon and B. Roldan Cuenya, *Chem. Soc. Rev.*, 2020, **49**, 6884–6946.

24 R. Gusmão, M. Veselý and Z. Sofer, *ACS Catal.*, 2020, **10**, 9634–9648.

25 Y. Wang, H. Su, Y. He, L. Li, S. Zhu, H. Shen, P. Xie, X. Fu, G. Zhou, C. Feng, D. Zhao, F. Xiao, X. Zhu, Y. Zeng, M. Shao, S. Chen, G. Wu, J. Zeng and C. Wang, *Chem. Rev.*, 2020, **120**, 12217–12314.

26 R. T. Hannagan, G. Giannakakis, M. Flytzani-Stephanopoulos and E. C. H. Sykes, *Chem. Rev.*, 2020, **120**, 12044–12088.

27 T. Zhang, A. G. Walsh, J. Yu and P. Zhang, *Chem. Soc. Rev.*, 2021, **50**, 569–588.

28 X. Wei, X. Luo, N. Wu, W. Gu, Y. Lin and C. Zhu, *Nano Energy*, 2021, **84**, 105817.

29 B. Qiao, A. Wang, X. Yang, L. F. Allard, Z. Jiang, Y. Cui, J. Liu, J. Li and T. Zhang, *Nat. Chem.*, 2011, **3**, 634–641.

30 W. Y. Zhang, Y. G. Chao, W. S. Zhang, J. H. Zhou, F. Lv, K. Wang, F. X. Lin, H. Luo, J. Li, M. P. Tong, E. K. Wang and S. J. Guo, *Adv. Mater.*, 2021, **33**, 2102576.

31 J. Liu, D. Cao, H. Xu and D. Cheng, *Nano Sel.*, 2021, **2**, 251–270.

32 H. Yan, Y. Lin, H. Wu, W. Zhang, Z. Sun, H. Cheng, W. Liu, C. Wang, J. Li, X. Huang, T. Yao, J. Yang, S. Wei and J. Lu, *Nat. Commun.*, 2017, **8**, 1070.

33 S. Tian, Q. Fu, W. Chen, Q. Feng, Z. Chen, J. Zhang, W.-C. Cheong, R. Yu, L. Gu, J. Dong, J. Luo, C. Chen, Q. Peng, C. Draxl, D. Wang and Y. Li, *Nat. Commun.*, 2018, **9**, 2353.

34 D. Cao, J. Wang, H. Xu and D. Cheng, *Small*, 2021, **17**, 2101163.

35 J. H. Kim, D. Shin, J. Lee, D. S. Baek, T. J. Shin, Y.-T. Kim, H. Y. Jeong, J. H. Kwak, H. Kim and S. H. Joo, *ACS Nano*, 2020, **14**, 1990–2001.

36 I. H. Kim, J. Lim and S. O. Kim, *Acc. Mater. Res.*, 2021, **2**, 394–406.

37 Z. Qiao, C. Wang, C. Li, Y. Zeng, S. Hwang, B. Li, S. Karakalos, J. Park, A. J. Kropf, E. C. Wegener, Q. Gong,

This journal is © The Royal Society of Chemistry 2022

J. Mater. Chem. A, 2022, **10**, 5673–5698 | **5695**

H. Xu, G. Wang, D. J. Myers, J. Xie, J. S. Spendelow and G. Wu, *Energy Environ. Sci.*, 2021, **14**, 4948–4960.

38 Y. He, Y. Li, J. Zhang, S. Wang, D. Huang, G. Yang, X. Yi, H. Lin, X. Han, W. Hu, Y. Deng and J. Ye, *Nano Energy*, 2020, **77**, 105010.

39 X. Wang, X. Sang, C.-L. Dong, S. Yao, L. Shuai, J. Lu, B. Yang, Z. Li, L. Lei, M. Qiu, L. Dai and Y. Hou, *Angew. Chem., Int. Ed.*, 2021, **60**, 11959–11965.

40 C. Shi, Y. Liu, R. Qi, J. Li, J. Zhu, R. Yu, S. Li, X. Hong, J. Wu, S. Xi, L. Zhou and L. Mai, *Nano Energy*, 2021, **87**, 106153.

41 Y. Ma, T. Yang, H. Zou, W. Zang, Z. Kou, L. Mao, Y. Feng, L. Shen, S. J. Pennycook, L. Duan, X. Li and J. Wang, *Adv. Mater.*, 2020, **32**, 2002177.

42 X. Cui, L. Gao, S. Lei, S. Liang, J. Zhang, C. D. Sewell, W. Xue, Q. Liu, Z. Lin and Y. Yang, *Adv. Funct. Mater.*, 2021, **31**, 2009197.

43 Y. Zhang, J. Li, J. Cai, L. Yang, T. Zhang, J. Lin, X. Wang, C. Chen, L. Zheng, C.-t. Au, B. Yang and L. Jiang, *ACS Catal.*, 2021, **11**, 4430–4440.

44 J. Liu, Z. Jin, X. Wang, J. J. Ge, C. P. Liu and W. Xing, *Sci. China: Chem.*, 2019, **62**, 669–683.

45 S. Paul, Y.-L. Kao, L. Ni, R. Ehnert, I. Herrmann-Geppert, R. van de Krol, R. W. Stark, W. Jaegermann, U. I. Kramm and P. Bogdanoff, *ACS Catal.*, 2021, **11**, 5850–5864.

46 N. K. Wagh, D.-H. Kim, S.-H. Kim, S. S. Shinde and J.-H. Lee, *ACS Nano*, 2021, **15**, 14683–14696.

47 X. Ao, W. Zhang, Z. Li, J.-G. Li, L. Soule, X. Huang, W.-H. Chiang, H. M. Chen, C. Wang, M. Liu and X. C. Zeng, *ACS Nano*, 2019, **13**, 11853–11862.

48 M. Liu, J. Lee, T.-C. Yang, F. Zheng, J. Zhao, C.-M. Yang and L. Y. S. Lee, *Small Methods*, 2021, **5**, 2001165.

49 N. Cheng, S. Stambula, D. Wang, M. N. Banis, J. Liu, A. Riese, B. Xiao, R. Li, T.-K. Sham, L.-M. Liu, G. A. Botton and X. Sun, *Nat. Commun.*, 2016, **7**, 13638.

50 E. Guan, J. Ciston, S. R. Bare, R. C. Runnebaum, A. Katz, A. Kulkarni, C. X. Kronawitter and B. C. Gates, *ACS Catal.*, 2020, **10**, 9065–9085.

51 Y. Yang, Y. Qian, H. Li, Z. Zhang, Y. Mu, D. Do, B. Zhou, J. Dong, W. Yan, Y. Qin, L. Fang, R. Feng, J. Zhou, P. Zhang, J. Dong, G. Yu, Y. Liu, X. Zhang and X. Fan, *Sci. Adv.*, 2020, **6**, eaba6586.

52 J. Gu, M. Z. Jian, L. Huang, Z. H. Sun, A. W. Li, Y. Pan, J. Z. Yang, W. Wen, W. Zhou, Y. Lin, H. J. Wang, X. Y. Liu, L. L. Wang, X. X. Shi, X. H. Huang, L. N. Cao, S. Chen, X. S. Zheng, H. B. Pan, J. F. Zhu, S. Q. Wei, W. X. Li and J. L. Lu, *Nat. Nanotechnol.*, 2021, **16**, 1141–1149.

53 R. Qin, K. Liu, Q. Wu and N. Zheng, *Chem. Rev.*, 2020, **120**, 11810–11899.

54 Y. Ying, X. Luo, J. Qiao and H. Huang, *Adv. Funct. Mater.*, 2021, **31**, 2007423.

55 Z. Y. Lu, B. F. Wang, Y. F. Hu, W. Liu, Y. F. Zhao, R. O. Yang, Z. P. Li, J. Luo, B. Chi, Z. Jiang, M. S. Li, S. C. Mu, S. J. Liao, J. J. Zhang and X. L. Sun, *Angew. Chem., Int. Ed.*, 2019, **58**, 2622–2626.

56 Z. P. Zeng, L. Y. Gan, H. B. Yang, X. Z. Su, J. J. Gao, W. Liu, H. Matsumoto, J. Gong, J. M. Zhang, W. Z. Cai, Z. Y. Zhang, Y. B. Yan, B. Liu and P. Chen, *Nat. Commun.*, 2021, **12**, 4088.

57 A. Han, X. J. Wang, K. Tang, Z. D. Zhang, C. L. Ye, K. J. Kong, H. B. Hu, L. R. Zheng, P. Jiang, C. X. Zhao, Q. Zhang, D. S. Wang and Y. D. Li, *Angew. Chem., Int. Ed.*, 2021, **60**, 19262–19271.

58 M. M. Tong, F. F. Sun, Y. Xie, Y. Wang, Y. Q. Yang, C. G. Tian, L. Wang and H. G. Fu, *Angew. Chem., Int. Ed.*, 2021, **60**, 14005–14012.

59 Y. S. Wei, L. M. Sun, M. Wang, J. H. Hong, L. L. Zou, H. W. Liu, Y. Wang, M. Zhang, Z. Liu, Y. W. Li, S. Horike, K. Suenaga and Q. Xu, *Angew. Chem., Int. Ed.*, 2020, **59**, 16013–16022.

60 J. Mao, J. Yin, J. Pei, D. Wang and Y. Li, *Nano Today*, 2020, **34**, 100917.

61 J. Han, J. Lu, M. Wang, Y. Wang and F. Wang, *Chin. J. Chem.*, 2019, **37**, 977–988.

62 Y. Pan, Y. Qian, X. Zheng, S.-Q. Chu, Y. Yang, C. Ding, X. Wang, S.-H. Yu and H.-L. Jiang, *Natl. Sci. Rev.*, 2020, **8**, nwaa224.

63 M. Ouyang, K. G. Papanikolaou, A. Boubnov, A. S. Hoffman, G. Giannakakis, S. R. Bare, M. Stamatakis, M. Flytzani-Stephanopoulos and E. C. H. Sykes, *Nat. Commun.*, 2021, **12**, 1549.

64 Y. Wang, L. Cao, N. J. Libretto, X. Li, C. Li, Y. Wan, C. He, J. Lee, J. Gregg, H. Zong, D. Su, J. T. Miller, T. Mueller and C. Wang, *J. Am. Chem. Soc.*, 2019, **141**, 16635–16642.

65 Y. Zhao, X. Liu, D. Chen, Z. Liu, Q. Yang, X. Lin, M. Peng, P. Liu and Y. Tan, *Sci. China Mater.*, 2021, **64**, 1900–1909.

66 Q. L. Wu, M. Luo, J. H. Han, W. Peng, Y. Zhao, D. C. Chen, M. Peng, J. Liu, F. M. F. de Groot and Y. W. Tan, *ACS Energy Lett.*, 2020, **5**, 192–199.

67 S. Luo, L. Zhang, Y. Liao, L. Li, Q. Yang, X. Wu, X. Wu, D. He, C. He, W. Chen, Q. Wu, M. Li, E. J. M. Hensen and Z. Quan, *Adv. Mater.*, 2021, **33**, 2008508.

68 J. Bok, S. Y. Lee, B.-H. Lee, C. Kim, D. L. T. Nguyen, J. W. Kim, E. Jung, C. W. Lee, Y. Jung, H. S. Lee, J. Kim, K. Lee, W. Ko, Y. S. Kim, S.-P. Cho, J. S. Yoo, T. Hyeon and Y. J. Hwang, *J. Am. Chem. Soc.*, 2021, **143**, 5386–5395.

69 P. Tieu, X. Yan, M. Xu, P. Christopher and X. Pan, *Small*, 2021, **17**, 2006482.

70 O. L. Krivanek, T. C. Lovejoy, N. Dellby, T. Aoki, R. W. Carpenter, P. Rez, E. Soignard, J. Zhu, P. E. Batson, M. J. Lagos, R. F. Egerton and P. A. Crozier, *Nature*, 2014, **514**, 209–212.

71 R. Ishikawa, E. Okunishi, H. Sawada, Y. Kondo, F. Hosokawa and E. Abe, *Nat. Mater.*, 2011, **10**, 278–281.

72 S. Lee, X.-G. Sun, A. A. Lubimtsev, X. Gao, P. Ganesh, T. Z. Ward, G. Eres, M. F. Chisholm, S. Dai and H. N. Lee, *Nano Lett.*, 2017, **17**, 2229–2233.

73 B. Wei, Z. Fu, D. Legut, T. C. Germann, S. Du, H. Zhang, J. S. Francisco and R. Zhang, *Adv. Mater.*, 2021, **33**, 2102595.

74 C. H. M. van Oversteeg, H. Q. Doan, F. M. F. de Groot and T. Cuk, *Chem. Soc. Rev.*, 2017, **46**, 102–125.

75 F. Maurer, J. Jelic, J. Wang, A. Gänzler, P. Dolcet, C. Wöll, Y. Wang, F. Studt, M. Casapu and J.-D. Grunwaldt, *Nat. Catal.*, 2020, **3**, 824–833.

76 R. Jin, M. Peng, A. Li, Y. Deng, Z. Jia, F. Huang, Y. Ling, F. Yang, H. Fu, J. Xie, X. Han, D. Xiao, Z. Jiang, H. Liu and D. Ma, *J. Am. Chem. Soc.*, 2019, **141**, 18921–18925.

77 J. C. Matsubu, V. N. Yang and P. Christopher, *J. Am. Chem. Soc.*, 2015, **137**, 3076–3084.

78 H. Wang, T. K. J. Köster, N. M. Trease, J. Ségalini, P.-L. Taberna, P. Simon, Y. Gogotsi and C. P. Grey, *J. Am. Chem. Soc.*, 2011, **133**, 19270–19273.

79 Y. Qian, Y. Liu, Y. Zhao, X. Zhang and G. Yu, *EcoMat*, 2020, **2**, e12014.

80 Z. He, K. He, A. W. Robertson, A. I. Kirkland, D. Kim, J. Ihm, E. Yoon, G.-D. Lee and J. H. Warner, *Nano Lett.*, 2014, **14**, 3766–3772.

81 X. Jiao, Z. Chen, X. Li, Y. Sun, S. Gao, W. Yan, C. Wang, Q. Zhang, Y. Lin, Y. Luo and Y. Xie, *J. Am. Chem. Soc.*, 2017, **139**, 7586–7594.

82 C. Ye, N. Zhang, D. Wang and Y. Li, *Chem. Commun.*, 2020, **56**, 7687–7697.

83 A. K. Datye, *J. Catal.*, 2003, **216**, 144–154.

84 J. Ge, D. Zhang, Y. Qin, T. Dou, M. Jiang, F. Zhang and X. Lei, *Appl. Catal., B*, 2021, **298**, 120557.

85 G. Sun, Z.-J. Zhao, R. Mu, S. Zha, L. Li, S. Chen, K. Zang, J. Luo, Z. Li, S. C. Purdy, A. J. Kropf, J. T. Miller, L. Zeng and J. Gong, *Nat. Commun.*, 2018, **9**, 4454.

86 W. Karim, C. Spreafico, A. Kleibert, J. Gobrecht, J. VandeVondele, Y. Ekinci and J. A. van Bokhoven, *Nature*, 2017, **541**, 68–71.

87 A. I. Frenkel, *Chem. Soc. Rev.*, 2012, **41**, 8163–8178.

88 J. C. Li, Y. Meng, L. L. Zhang, G. Z. Li, Z. C. Shi, P. X. Hou, C. Liu, H. M. Cheng and M. H. Shao, *Adv. Funct. Mater.*, 2021, **31**, 2103360.

89 H. Wang, Q. Luo, W. Liu, Y. Lin, Q. Guan, X. Zheng, H. Pan, J. Zhu, Z. Sun, S. Wei, J. Yang and J. Lu, *Nat. Commun.*, 2019, **10**, 4998.

90 C. Wu, X. Zhang, Z. Xia, M. Shu, H. Li, X. Xu, R. Si, A. I. Rykov, J. Wang, S. Yu, S. Wang and G. Sun, *J. Mater. Chem. A*, 2019, **7**, 14001–14010.

91 J. Wang, Z. Huang, W. Liu, C. Chang, H. Tang, Z. Li, W. Chen, C. Jia, T. Yao, S. Wei, Y. Wu and Y. Li, *J. Am. Chem. Soc.*, 2017, **139**, 17281–17284.

92 D. M. Kolb and F. C. Simeone, *Electrochim. Acta*, 2005, **50**, 2989–2996.

93 J. Schnaidt, S. Beckord, A. K. Engstfeld, J. Klein, S. Brimaud and R. J. Behm, *Phys. Chem. Chem. Phys.*, 2017, **19**, 4166–4178.

94 S. Zhu, T. Li, W.-B. Cai and M. Shao, *ACS Energy Lett.*, 2019, **4**, 682–689.

95 A. Vizintin, J. Bitenc, A. Kopač Lautar, K. Pirnat, J. Grdadolnik, J. Stare, A. Randon-Vitanova and R. Dominko, *Nat. Commun.*, 2018, **9**, 661.

96 R. Alcántara, G. F. Ortiz, P. Lavela, J. L. Tirado, R. Stoyanova and E. Zhecheva, *Chem. Mater.*, 2006, **18**, 2293–2301.

97 X. Zheng, P. Li, S. Dou, W. Sun, H. Pan, D. Wang and Y. Li, *Energy Environ. Sci.*, 2021, **14**, 2809–2858.

98 Z. W. Seh, J. Kibsgaard, C. F. Dickens, I. Chorkendorff, J. K. Nørskov and T. F. Jaramillo, *Science*, 2017, **355**, eaad4998.

99 S. Chu and A. Majumdar, *Nature*, 2012, **488**, 294–303.

100 M. Shao, Q. Chang, J.-P. Dodelet and R. Chenitz, *Chem. Rev.*, 2016, **116**, 3594–3657.

101 B. Lu, Q. Liu and S. Chen, *ACS Catal.*, 2020, **10**, 7584–7618.

102 X. Li, L. Liu, X. Ren, J. Gao, Y. Huang and B. Liu, *Sci. Adv.*, 2020, **6**, eabb6833.

103 X. Li, Y. Zeng, C.-W. Tung, Y.-R. Lu, S. Baskaran, S.-F. Hung, S. Wang, C.-Q. Xu, J. Wang, T.-S. Chan, H. M. Chen, J. Jiang, Q. Yu, Y. Huang, J. Li, T. Zhang and B. Liu, *ACS Catal.*, 2021, **11**, 7292–7301.

104 Z. Zhang, C. Feng, X. Li, C. Liu, D. Wang, R. Si, J. Yang, S. Zhou and J. Zeng, *Nano Lett.*, 2021, **21**, 4795–4801.

105 H. Su, W. Zhou, W. Zhou, Y. Li, L. Zheng, H. Zhang, M. Liu, X. Zhang, X. Sun, Y. Xu, F. Hu, J. Zhang, T. Hu, Q. Liu and S. Wei, *Nat. Commun.*, 2021, **12**, 6118.

106 X. Guo, J. Gu, S. Lin, S. Zhang, Z. Chen and S. Huang, *J. Am. Chem. Soc.*, 2020, **142**, 5709–5721.

107 L. L. Han, Z. H. Ren, P. F. Ou, H. Cheng, N. Rui, L. L. Lin, X. J. Liu, L. C. Zhuo, J. Song, J. Q. Sun, J. Luo and H. L. L. Xin, *Angew. Chem., Int. Ed.*, 2021, **60**, 345–350.

108 M. B. Ross, P. De Luna, Y. Li, C.-T. Dinh, D. Kim, P. Yang and E. H. Sargent, *Nat. Catal.*, 2019, **2**, 648–658.

109 R. Daiyan, W. H. Saputera, H. Masood, J. Leverett, X. Lu and R. Amal, *Adv. Energy Mater.*, 2020, **10**, 1902106.

110 S. Zhang, Q. Fan, R. Xia and T. J. Meyer, *Acc. Chem. Res.*, 2020, **53**, 255–264.

111 D. Raciti and C. Wang, *ACS Energy Lett.*, 2018, **3**, 1545–1556.

112 Y. Wang, J. Liu, Y. Wang, A. M. Al-Enizi and G. Zheng, *Small*, 2017, **13**, 1701809.

113 B. Zhang, B. Zhang, Y. Jiang, T. Ma, H. Pan and W. Sun, *Small*, 2021, **17**, 2101443.

114 F. Li, D. Chen, L.-H. Zhang, J. Du, H. Wang, J. Guo, J. Zhan and F. Yu, *Angew. Chem., Int. Ed.*, 2021, **60**, 24022–24027.

115 M. M. Feng, X. M. Wu, H. Y. Cheng, Z. H. Fan, X. C. Li, F. J. Cui, S. Fan, Y. Dai, G. P. Lei and G. H. He, *J. Mater. Chem. A*, 2021, **9**, 23817–23827.

116 T. Ding, X. K. Liu, Z. N. Tao, T. Y. Liu, T. Chen, W. Zhang, X. Y. Shen, D. Liu, S. C. Wang, B. B. Pang, D. Wu, L. L. Cao, L. Wang, T. Liu, Y. F. Li, H. T. Sheng, M. Z. Zhu and T. Yao, *J. Am. Chem. Soc.*, 2021, **143**, 11317–11324.

117 N. Q. Zhang, X. X. Zhang, Y. K. Kang, C. L. Ye, R. Jin, H. Yan, R. Lin, J. R. Yang, Q. Xu, Y. Wang, Q. H. Zhang, L. Gu, L. C. Liu, W. Y. Song, J. Liu, D. S. Wang and Y. D. Li, *Angew. Chem., Int. Ed.*, 2021, **60**, 13388–13393.

118 W. J. Zhu, L. Zhang, S. H. Liu, A. Li, X. T. Yuan, C. L. Hu, G. Zhang, W. Y. Deng, K. T. Zang, J. Luo, Y. M. Zhu, M. Gu, Z. J. Zhao and J. L. Gong, *Angew. Chem., Int. Ed.*, 2020, **59**, 12664–12668.

119 M.-J. Cheng, E. L. Clark, H. H. Pham, A. T. Bell and M. Head-Gordon, *ACS Catal.*, 2016, **6**, 7769–7777.

120 H. Xie, Y. Y. Wan, X. M. Wang, J. S. Liang, G. Lu, T. Y. Wang, G. L. Chai, N. M. Adli, C. Priest, Y. H. Huang, G. Wu and Q. Li, *Appl. Catal., B*, 2021, **289**, 119783.

121 H. Zhang, S. Hwang, M. Wang, Z. Feng, S. Karakalos, L. Luo, Z. Qiao, X. Xie, C. Wang, D. Su, Y. Shao and G. Wu, *J. Am. Chem. Soc.*, 2017, **139**, 14143–14149.

This journal is © The Royal Society of Chemistry 2022

J. Mater. Chem. A, 2022, **10**, 5673–5698 | **5697**

122 Y. Han, Y.-G. Wang, W. Chen, R. Xu, L. Zheng, J. Zhang, J. Luo, R.-A. Shen, Y. Zhu, W.-C. Cheong, C. Chen, Q. Peng, D. Wang and Y. Li, *J. Am. Chem. Soc.*, 2017, **139**, 17269–17272.

123 W. Xie, Y. Song, S. Li, J. Li, Y. Yang, W. Liu, M. Shao and M. Wei, *Adv. Funct. Mater.*, 2019, **29**, 1906477.

124 Z. Wang, C. Zhu, H. Tan, J. Liu, L. Xu, Y. Zhang, Y. Liu, X. Zou, Z. Liu and X. Lu, *Adv. Funct. Mater.*, 2021, **31**, 2104735.

125 R. Gao, J. Wang, Z.-F. Huang, R. Zhang, W. Wang, L. Pan, J. Zhang, W. Zhu, X. Zhang, C. Shi, J. Lim and J.-J. Zou, *Nat. Energy*, 2021, **6**, 614–623.

126 Z. Zhu, H. Yin, Y. Wang, C.-H. Chuang, L. Xing, M. Dong, Y.-R. Lu, G. Casillas-Garcia, Y. Zheng, S. Chen, Y. Dou, P. Liu, Q. Cheng and H. Zhao, *Adv. Mater.*, 2020, **32**, 2004670.

127 L. Zhang, H. Liu, S. Liu, M. Norouzi Banis, Z. Song, J. Li, L. Yang, M. Markiewicz, Y. Zhao, R. Li, M. Zheng, S. Ye, Z.-J. Zhao, G. A. Botton and X. Sun, *ACS Catal.*, 2019, **9**, 9350–9358.

128 G. Zhao, K. Rui, S. X. Dou and W. Sun, *Adv. Funct. Mater.*, 2018, **28**, 1803291.

129 H. Jin, X. Liu, S. Chen, A. Vasileff, L. Li, Y. Jiao, L. Song, Y. Zheng and S.-Z. Qiao, *ACS Energy Lett.*, 2019, **4**, 805–810.

130 A. A. Peterson and J. K. Nørskov, *J. Phys. Chem. Lett.*, 2012, **3**, 251–258.

131 S. Ye, F. Luo, Q. Zhang, P. Zhang, T. Xu, Q. Wang, D. He, L. Guo, Y. Zhang, C. He, X. Ouyang, M. Gu, J. Liu and X. Sun, *Energy Environ. Sci.*, 2019, **12**, 1000–1007.

132 K. Jiang, B. Liu, M. Luo, S. Ning, M. Peng, Y. Zhao, Y.-R. Lu, T.-S. Chan, F. M. F. de Groot and Y. Tan, *Nat. Commun.*, 2019, **10**, 1743.

133 J. Yu, J. Li, C.-Y. Xu, Q. Liu, J. Liu, R. Chen, J. Zhu, R. Li and J. Wang, *Carbon*, 2021, **185**, 96–104.

134 P. P. Su, W. Pei, X. W. Wang, Y. F. Ma, Q. K. Jiang, J. Liang, S. Zhou, J. J. Zhao, J. Liu and G. Q. Lu, *Angew. Chem., Int. Ed.*, 2021, **60**, 16044–16050.

135 C.-H. Chen, D. Wu, Z. Li, R. Zhang, C.-G. Kuai, X.-R. Zhao, C.-K. Dong, S.-Z. Qiao, H. Liu and X.-W. Du, *Adv. Energy Mater.*, 2019, **9**, 1803913.

136 N.-T. Suen, S.-F. Hung, Q. Quan, N. Zhang, Y.-J. Xu and H. M. Chen, *Chem. Soc. Rev.*, 2017, **46**, 337–365.

137 M. Tahir, L. Pan, F. Idrees, X. Zhang, L. Wang, J.-J. Zou and Z. L. Wang, *Nano Energy*, 2017, **37**, 136–157.

138 L. Bai, C.-S. Hsu, D. T. L. Alexander, H. M. Chen and X. Hu, *J. Am. Chem. Soc.*, 2019, **141**, 14190–14199.

139 Y. C. Yao, S. L. Hu, W. X. Chen, Z. Q. Huang, W. C. Wei, T. Yao, R. R. Liu, K. T. Zang, X. Q. Wang, G. Wu, W. J. Yuan, T. W. Yuan, B. Q. Zhu, W. Liu, Z. J. Li, D. S. He, Z. G. Xue, Y. Wang, X. S. Zheng, J. C. Dong, C. R. Chang, Y. X. Chen, X. Hong, J. Luo, S. Q. Wei, W. X. Li, P. Strasser, Y. E. Wu and Y. D. Li, *Nat. Catal.*, 2019, **2**, 304–313.

140 H. Su, L. Chen, Y. Chen, R. Si, Y. Wu, X. Wu, Z. Geng, W. Zhang and J. Zeng, *Angew. Chem., Int. Ed.*, 2020, **59**, 20411–20416.

141 G.-F. Chen, S. Ren, L. Zhang, H. Cheng, Y. Luo, K. Zhu, L.-X. Ding and H. Wang, *Small Methods*, 2019, **3**, 1800337.

142 G. Qing, R. Ghazfar, S. T. Jackowski, F. Habibzadeh, M. M. Ashtiani, C.-P. Chen, M. R. Smith and T. W. Hamann, *Chem. Rev.*, 2020, **120**, 5437–5516.

143 X. Guo, H. Du, F. Qu and J. Li, *J. Mater. Chem. A*, 2019, **7**, 3531–3543.

144 Y. Li, J. Li, J. Huang, J. Chen, Y. Kong, B. Yang, Z. Li, L. Lei, G. Chai, Z. Wen, L. Dai and Y. Hou, *Angew. Chem., Int. Ed.*, 2021, **60**, 9078–9085.

145 S. T. Li, A. V. Nagarajan, D. R. Alfonso, M. K. Sun, D. R. Kauffman, G. Mpourmpakis and R. C. Jin, *Angew. Chem. Int. Ed.*, 2021, **60**, 6351–6356.

146 Q. He, D. Liu, J. H. Lee, Y. Liu, Z. Xie, S. Hwang, S. Kattel, L. Song and J. G. Chen, *Angew. Chem. Int. Ed.*, 2020, **59**, 3033–3037.

147 W. Ren, X. Tan, W. Yang, C. Jia, S. Xu, K. Wang, S. C. Smith and C. Zhao, *Angew. Chem. Int. Ed.*, 2019, **58**, 2622–2626.

148 M. Zhang, Z. Zhang, Z. Zhao, H. Huang, D. H. Anjum, D. Wang, J.-h. He and K.-W. Huang, *ACS Catal.*, 2021, **11**, 11103–11108.

149 X. Wei, S. Song, N. Wu, X. Luo, L. Zheng, L. Jiao, H. Wang, Q. Fang, L. Hu, W. Gu, W. Song and C. Zhu, *Nano Energy*, 2021, **84**, 105840.

150 B. Hu, A. Huang, X. Zhang, Z. Chen, R. Tu, W. Zhu, Z. Zhuang, C. Chen, Q. Peng and Y. Li, *Nano Res.*, 2021, **14**, 3482–3488.

151 M. Xiao, H. Zhang, Y. Chen, J. Zhu, L. Gao, Z. Jin, J. Ge, Z. Jiang, S. Chen, C. Liu and W. Xing, *Nano Energy*, 2018, **46**, 396–403.

152 R. Zhao, Z. B. Liang, S. Gao, C. Yang, B. J. Zhu, J. L. Zhao, C. Qu, R. Q. Zou and Q. Xu, *Angew. Chem. Int. Ed.*, 2019, **58**, 1975–1979.

153 J. S. Jirkovský, I. Panas, E. Ahlberg, M. Halasa, S. Romani and D. J. Schiffrin, *J. Am. Chem. Soc.*, 2011, **133**, 19432–19441.

154 J. J. Gao, P. Du, Q. H. Zhang, X. Shen, F. K. Chiang, Y. R. Wen, X. Lin, X. J. Liu and H. J. Qiu, *Electrochim. Acta*, 2019, **297**, 155–162.

155 T. He, A. R. Puente Santiago and A. Du, *J. Catal.*, 2020, **388**, 77–83.